Detecting parametric resonance in a floating oscillating water column device for wave energy conversion: Numerical simulations and validation with physical model tests

Applied Energy 276 (2020) 115421

Contents lists available at ScienceDirect

Applied Energy

journal homepage: www.elsevier.com/locate/apenergy

Detecting parametric resonance in a floating oscillating water column device for wave energy conversion: Numerical simulations and validation with physical model tests

Giuseppe Giorgi[a,*], Rui P.F. Gomes[b], João C.C. Henriques[b], Luís M.C. Gato[b], Giovanni Bracco[a], Giuliana Mattiazzo[a]

[a] Department of Mechanical and Aerospace Engineering, Polytechnic University of Turin, 10129 Torino, Italy
[b] IDMEC, Instituto Superior Técnico, Universidade de Lisboa, Av. Rovisco Pais 1, 1049-001 Lisboa, Portugal

HIGHLIGHTS

- A bottom-moored Spar-buoy OWC is simulated using a nonlinear Froude-Krylov model.
- Drag forces due to real fluid effects are estimated using experimental data.
- The numerical model detects the occurrence of parametric resonance in pitch & roll.
- Numerical results are validated using model-scale experiments in a wave tank.
- Parametric resonance shows a reduction in energy conversion efficiency up to 53%.

ARTICLE INFO

Keywords:
Ocean wave energy
Floating oscillating water column
Spar-buoy OWC
Nonlinear Froude-Krylov model
Experimental tests
Roll and pitch parametric resonance

ABSTRACT

The wave energy sector has faced enormous technological improvements over the last five decades, however, due to the complexity of the hydrodynamic processes, current numerical models still have limitations in predicting relevant phenomena. In particular, floating spar-type wave energy converters are prone to large undesirable roll and pitch amplitudes caused by a dynamic instability induced by parametric resonance. Detecting this phenomenon accurately is essential as it impacts drastically on power extraction, structural loads and mooring forces. This paper presents the validation of results from a numerical model, capable of detecting parametric resonance, using experimental data. Experiments were carried out for a scaled model of the Spar-buoy OWC (Oscillating Water Column) device at a large ocean basin. The buoy uses a slack-mooring system attached to the basin floor. The scaled turbine damping effect is simulated by a calibrated orifice plate. Two different buoy draft configurations are considered to analyse the effect of different mass distributions. The numerical model considers the nonlinear Froude-Krylov forces, which allows it to capture complex hydrodynamic phenomena associated with the six-degree-of-freedom motion of the buoy. The mooring system is simulated through a quasi-static inelastic line model. Real fluid effects are accounted for through drag forces based on the Morison's equation and determined from experimental data. The comparison of results from regular-wave tests shows good agreement, including when parametric resonance is detected. Numerical results show that parametric resonance can produce a negative impact on power extraction efficiency up to 53%.

1. Introduction

Parametric resonance is a nonlinear phenomenon that can occur in dynamic systems, and is characterized by not being externally induced [1]. The occurrence of parametrically excited motions in ocean engineering applications has motivated its research in this area [2]. Historically, it became relevant due to its influence on the stability of containerships [3], which can cause large roll angles and, consequently, the damage of the ship and its cargo. Criteria [4] and models [5] for containers have been developed. Spar platforms, typical of deep water applications, are also prone to parametric resonance [6], in conventional spars [7] as well as deep draft multi-spar [8]. When they are

* Corresponding author.
E-mail address: giuseppe.giorgi@polito.it (G. Giorgi).

https://doi.org/10.1016/j.apenergy.2020.115421
Received 27 February 2020; Received in revised form 5 June 2020; Accepted 19 June 2020

subject to large heave amplitudes due to wave action, the stability characteristics are affected, and pitch and roll can become internally excited. The occurrence of parametric resonance is also observed in wave energy converters (WECs), which are recently attracting greater interest to diversify the renewable energy mix [9]. It is more commonly detected in heaving spar-type devices, and has the consequence of inducing large undesirable roll and pitch amplitudes, which impacts negatively on the WEC power extraction. This phenomenon has been identified in the wave-tank testing of several heaving WECs, and it is more notably relevant for devices that are designed to perform with large heave motions: a floating cylindrical OWC (Oscillating Water Column) [10], a free-floating sloped device [11], a self-reacting 2-body device [12], and on a prototype of the Spar-buoy device, without [13] and with [14] fins to limit instability. The numerical simulation of this phenomenon requires a model capable of dealing with nonlinear hydrodynamics effects. Even though this type of model is not commonly used for the performance evaluation of WECs, a few addressed this issue: with a panel-meshed approach for the SEAREV [15] and Wavebob [12] devices; with an analytical approach for a Sparbuoy-like [16] and a single point absorber [17] device; through computational fluid dynamics [18]. However, the comparison with validation of these results is still scarce in the literature. In heaving WECs, parametric excited motions in roll and pitch can occur when the metacentric height presents a time-varying amplitude that affect the restoring characteristics in those modes [7]. Those motions are internally excited if the incident wave frequency is near or at twice the value of the corresponding natural frequency. The amount of damping present in the system limits the amplitude of the internally excited motion. Furthermore, a similar effect can be observed due to instantaneous pressure variations on the WEC wetted surface [6].

In this paper, we focus our research on a floating oscillating water column WEC with axisymmetric geometry, the Spar-buoy OWC, which can be installed far from [19] or close to [20] a breakwater. In general, a floating OWC device consists of a semi-submerged structure with an inner hollow section [21], opened to the sea water and connected to the exterior atmosphere through an air turbine [22]. The volume of water moving inside the hollow section is known as the OWC. The wave action generate motions on the buoy and on the OWC, which creates cyclic compressions and expansions of the volume of the air chamber above the inner free surface, forcing an airflow through the turbine. Since the airflow is bidirectional, a turbine with self-rectifying characteristics is required [23]. In the case of the Spar-buoy OWC, the device is characterized by a floating module connected to a vertical hollow tube where the OWC and air chamber are located. This concept was initially developed in the 1940s for small navigation buoys, providing initial framework for analysis [24], experiment [25] and design [26]. The possibility of applying this technology in large arrays at offshore locations, where more space and more energy are available, makes it an option with large potential for extensive production of electricity. Geometry and turbine optimizations of this device, for maximizing power extraction, were reported in the literature: [27] focuses on performance evaluation, [28] on hydrodynamic optimization, [29] on the conversion principle and turbine characteristics, and [30] on empirical models for stationary OWC. Efficient designs required a combination between the inertia of the buoy and of the OWC, with a tendency for the OWC having the largest possible inertia and the buoy having large heave amplitudes. Two relevant operational conditions were identified for the turbine. The first one refers to a turbine with a low damping effect, where efficient energy conversion occurs near the buoy and OWC heave natural frequencies. The second one is associated with an high damping condition, the relative motions between the buoy and OWC are small and efficient energy absorption is observed at a frequency between the buoy and OWC heave natural frequencies. For simulations with a real wave climate, the optimal turbine damping effect was found to be between the two options above, where a large range of frequencies presented a relatively good energy absorption [28]. One of the optimum geometries obtained in [28] was tested at model scale in a wave flume, with the buoy limited to oscillate only in heave [31]. Damping due to real fluid effects were determined from regular wave tests. The same geometry was tested with a slack-mooring system in a wave flume [32], and in wave tank at a larger scale [13]. The occurrence of parametric roll and pitch resonance was identified in those experiments. An experimental study, at a small scale, on the reduction of parametrically excited motions was carried out by applying vertical fins, in the radial direction, on the exterior surfaces [14]. The fins showed an increase of the damping effect but they did not significantly reduced the amplitudes of the parametrically excited motions.

In this paper we study the occurrence of parametric resonance in roll and pitch in a Spar-buoy OWC device equipped with a three-line slack-mooring system. Data from regular wave experimental tests is used to validate results from a nonlinear Froude-Krylov model. Two buoy configurations, with different draft and mass distribution, are analysed. The comparison of the numerical results with simplified analytical solutions is carried out. The impact of roll and pitch parametric resonance on the power conversion efficiency is evaluated. The conclusion summarizes our findings and presents discussion on the advantages and limitations of the numerical model.

2. Occurrence of parametric resonance

Parametric resonance in floating spar-type structures is a nonlinear phenomenon that induces a dynamic instability in the device, which can result in large roll and pitch motions. The large motions on these modes occur even when they are not being excited externally by incoming waves, as long as the ideal conditions are present. To explain this phenomenon, let us consider a device with axisymmetric geometry, with a reference frame at the free surface, where the x-axis has the same direction as the wave propagation and the z-axis is vertical and pointing upwards. The translations on the direction of x-, y- and z-axis are named as surge x_1, sway x_2 and heave x_3, respectively. The rotations over the same axes are denominated as roll x_4, pitch x_5 and yaw x_6. Due to symmetry, the device is only excited by waves in surge, heave and pitch. However, due to the dynamic instability, motion can be induced in all six modes. To understand this effect, we consider the uncoupled roll motion equation,

$$(M_{44} + A_{44})\frac{d^2x_4}{dt^2} + B_{44}\frac{dx_4}{dt} + \rho g V \overline{GM} x_4 = 0, \tag{1}$$

where M_{44} is the inertia coefficient, A_{44} is the radiation added inertia coefficient, B_{44} is a linearised damping coefficient, which includes damping due to wave radiation and viscous effects. The term $\rho g V \overline{GM}$ in Eq. (1) represents the hydrostatic stiffness in roll (as a consequence of symmetry, the same term is applicable for pitch), where ρ is the water density, g is the acceleration of gravity, V is the buoy displaced volume, and $\overline{GM}$ is the metacentric height. By definition [33], the natural frequency in roll $\omega_{n,4}$ is given by

$$\omega_{n,4}^2 = \frac{\rho g V \overline{GM}}{M_{44} + A_{44}}, \tag{2}$$

with M_{44} and A_{44} taken relative to the centre of gravity.

The $\overline{GM}$ is an indicator of static stability in floating structures [34]. For static stability, $\overline{GM}$ needs to be higher than zero. Note that V and $\overline{GM}$ can vary over time when buoy oscillates, particularly when the motion is in heave. It follows that the hydrostatic stiffness in the roll DoF (K_4) is time-dependent, since it is defined as:

$$K_4(t) = \rho g V(t) \overline{GM}(t). \tag{3}$$

The K_4 variation is associated with the changes of the centre of buoyancy, waterplane area, and submerged volume. Considering that the buoy is excited by a monochromatic wave with frequency ω, the induced heave motion produces a sinusoidal variation of K_4 over time,

which can be described by

$$K_4(t) = \overline{K_4}(1 + \epsilon \cos\omega t), \tag{4}$$

where $\overline{K_4}$ is the hydrostatics stiffness in still water conditions and ϵ is the dimensionless amplitude of the hydrostatic stiffness variations, $\epsilon = (K_{4,\max} - K_{4,\min})/(2\overline{K_4})$. The parameters $K_{4,\max}$ and $K_{4,\min}$ represent the maximum and minimum values of K_4 over a wave cycle. By considering $\tau = \omega t$, $\mu = B_{44}(\omega(M_{44} + A_{44}))$, $\Delta = (\omega_{n,4}/\omega)^2$ and $\Lambda = \epsilon\,\Delta$, we can rewrite Eq. (1) as

$$\frac{d^2x_4}{d\tau^2} + \mu\frac{dx_4}{d\tau} + (\Delta + \Lambda\cos\tau)x_4 = 0. \tag{5}$$

Eq.(5) is known as the damped Mathieu equation, a particular case of the Hill differential equation [35].In the case of damping being zero ($\mu = 0$), the equation becomes the Mathieu differential equation.For some combination of Δ and Λ values, the solution of Eq.(5) is unstable.In practice, it means that the floating structure becomes dynamically unstable in roll, and therefore subject to parametric resonance.As a consequence, the roll amplitude increases over time in the absence of any external excitation until a threshold value is reached, which is normally achieved by the balance with other nonlinear phenomena (e.g., variation of the waterplane area or damping from viscous fluid effects).Stability diagrams, defined as Δ versus Λ, are used to identify the unstable regions.Using a perturbation method (see e.g. [36]), it is possible to determine the limits of stability of this equation.These curves are calculated through a power series expansion $\Delta = n^2/4 + \Delta_1\Lambda + \Delta_2\Lambda^2 + \Delta_3\Lambda^3 + \mathcal{O}(\Lambda^4)$, where n is the order of the parametric peak and Δ_i are the power series coefficients (for $i = 1, 2, \ldots$).Fig.1 presents a stability diagram for a Spar-buoy OWC device, presenting the two most significant zones of instability.The first zone is observed in the vicinity of $\Delta = 1/4$, which corresponds to $\omega = 2\omega_{n,4}$.The range of values of Δ covered by the instability region tends to increase with the increase of Λ.This implies that cases with larger K_4 amplitude display a larger range of frequencies that can induce unstable motions.The second zone, appears near $\Delta = 1$, i.e.near the roll natural frequency ($\omega = \omega_{n,4}$).In Fig.1, the limits of stability for $\mu = 0$ are obtained by considering a 6th-order power series expansion of Δ. The curves with $\mu \neq 0$ are represented by a 1st-order approximation of Δ for the curves in the vicinity of $\Delta = 1/4$ ($n = 1$) and by a 2nd-order approximation of Δ for the curve in the vicinity of $\Delta = 1$ ($n = 2$). In addition, two curves are shown, representing the constant values of dimensionless hydrostatic stiffness amplitude variation ϵ over a large range of frequencies.

Typical deep-water spar platforms used in the oil and gas industry have the pitch/roll and heave natural periods around 60 s and 30 s, respectively [7]. The relation between these natural periods make these

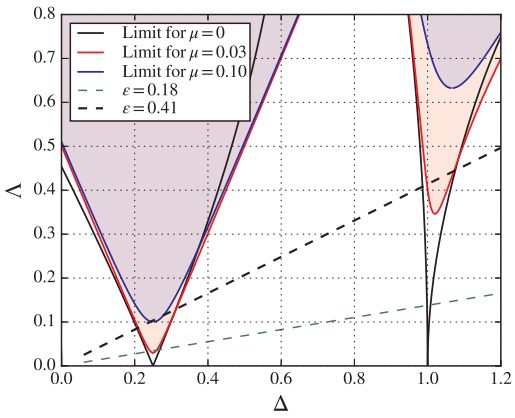

Fig. 1. Stability diagram for detecting the occurrence of parametric resonance, for different values of dimensionless damping μ. The shaded zones represent the unstable regions. The dashed lines show curves with constant dimensionless metacentric height amplitude ϵ.

platforms prone to parametric resonance in roll when they are excited by long swells around 30 s, as heave can be highly amplified due to resonance, and the conditions for the first instability zone of Fig. 1 are reached. In the case of these platforms, damping heave plates can be used to prevent large heave amplitudes and mitigate the occurrence of parametric resonance.

In the case of spar-type wave energy converters, the heave natural period of the device is within the typical wave frequency for efficient energy absorption (8–12 s) [32]. The roll/pitch natural period is around (15–25 s), i.e., near the condition $\omega = 2\omega_{n,4}$ of the first instability zone. Up to date, there are no effective methods to mitigate parametric resonance in spar-type wave energy converters. In addition, the application of damping heave plates is not convenient, since in addition to reduce heave amplitudes, they would also reduce the wave energy absorption efficiency.

The use of a one-degree-of-freedom model, as the one described in Eq. (5), allows detecting the occurrence of the parametric resonance. This model is helpful at an initial development stage to avoid design configurations that could be prone to this dynamic instability. However, to study complex motion couplings in 6 degree-of-freedom systems, which include mooring lines and power take-off systems, and to evaluate the level of magnitude of this dynamic instability, a more effective model is required, as the one that is presented in this paper. An additional advantage of using a 6 degree-of-freedom model is the evaluation of the nonlinear Froude-Krylov pressure variations on the device hull, which can induce instability in a similar way as the hydrostatic stiffness variation [6].

In axisymmetric geometries, transverse modes subject to unidirectional waves, such as roll and sway, are not externally excited. Since parametric resonance occurs due to an instability, an asymmetry in the time-domain solution is required to allow the roll motion to settle. In general, this is done by considering an initial condition slightly different from zero, which will provide an initial energy to this state. The small roll perturbation will be magnified if the conditions are adequate. Due to the unstable and nonlinear behaviour of these problems, the initial conditions may influence the settling of the permanent regime. Therefore, it is important to verify if the solution depends on the system initial conditions [12].

3. Experimental setup

The experimental testing of an 1:32nd-scale model of the Spar-buy OWC was carried out at the COAST laboratory ocean basin (Plymouth, UK). The basin is 15.5 m wide, 35 m long and has the possibility of adjusting the water depth up to 3 m through the use of a movable floor. For the testing of the isolated Spar-buoy OWC model, a water depth of 2.5 m was considered, corresponding to 80 m at full scale. The wave generation system consists of 24 individually controlled hinged flap paddles with wave absorption capability. The dissipative beach has a convex shape for a better wave absorption performance. Only regular and long-crested waves are considered in this work.

The experiments were designed by adopting the Froude scaling criterion [37]. The Spar-buoy OWC geometry was based on the 16 m diameter and 48 m draft device optimized for a wave climate from a location off the Portuguese western coast [28]. A a perspective view of the model is shown in Fig. 2. The cylindrical and conical surfaces were built from welded steel plates, whereas the toroidal shape at the bottom was made of concrete using a steel mesh. The latter part represented the fixed ballast section. Above it, a variable ballast section allowed the adjustment of the model mass by adding or removing steel plates. This flexibility allowed the testing of model configurations with different drafts and mass distributions At the top of the air chamber, an orifice plate was used to replicate the turbine damping effect at model scale. Three pulleys were fixed to the exterior surface of the buoy near the free surface, which functioned as the fairleads for the mooring lines. Each mooring line was attached to a S-beam load cell at the top of the device

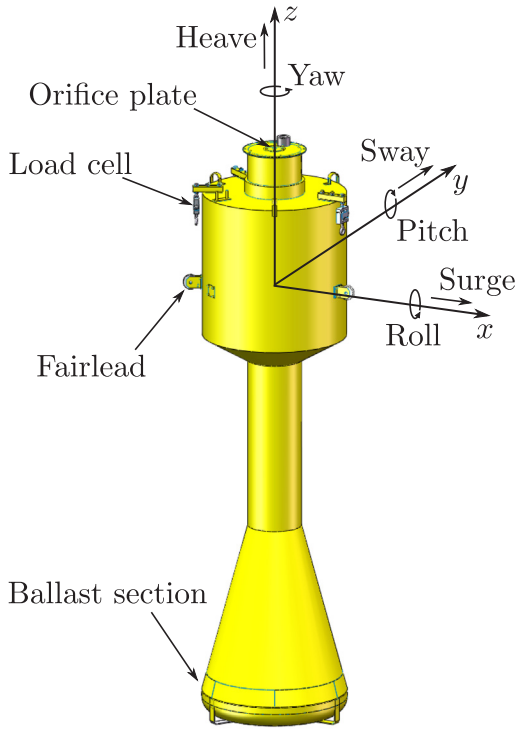

Fig. 2. Three-dimensional representation of the Spar-buoy OWC model, relevant components, reference frame in still water conditions, and oscillating modes.

and fitted to the inner part of the fairlead. This configuration allowed the assessment of the mooring line tension at the fairlead through an axial force measurement. The mooring lines were anchored on the floor through heavy concrete blocks.

Fig. 4 shows a schematic representation of the wave tank with the position of the model in the experiments. Eight resistive wave gauges (WG1, WG2, …, WG8) were used to measure the free surface elevation on different positions in the tank. Wave gauge WG8, positioned aside the device, was used to determine the incident wave conditions at the device location, i.e., already accounting for reflections on the absorption beach. The measurements of this wave gauge were compared with the ones from a wave gauge at the device location in its absence. Since small differences were found, WG8 was considered as an adequate proxy.

For the analysis of the device performance several parameters were measured. These included the motion of the device, the air pressure difference inside the air chamber, the displacement of the OWC relative to the buoy, the loads on the mooring lines, and the incident wave conditions. The data acquisition system was placed near the device using a gantry platform positioned above the device. All data were captured with the same time reference. The six-degree-of-freedom motion of the buoy was recorded using a motion-tracking system Oqus300+ developed by Qualisys. This system uses the measurements of several reflective targets attached to the buoy, via six infrared cameras placed around the basin, to detect the motion in each degree of freedom. The relative motion between the OWC and the buoy was measured by an ultrasonic sensor TSPC-30S1–232 manufactured by SENIX. The sensor, fixed to the top of the air chamber and facing the free surface, was able to measure displacements from 110 mm to 4000 mm. The tensions on the mooring lines at the fairlead were measured by three S-beam load cells, DBBSM-25Kg-003–017 manufactured by Applied Measurements Ltd, with a measurement range between 0 and 250 N. The air pressure difference between the air chamber and the atmosphere was measured by a ultra low pressure sensor installed on the buoy. The differential pressure sensor

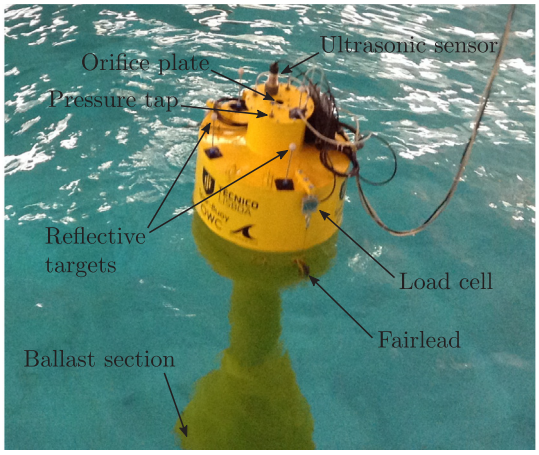

Fig. 3. View of the model from the gantry platform, with identification of model components.

DC010NDC4, developed by Honeywell, had a range between −2500 and 2500 Pa. Four pressure taps, installed on the top of the air chamber, were connected to the sensor though flexible plastic tubes. The mass flow rate through the orifice was determined from the pressure difference signal by applying the flow-rate-versus-pressure-drop relationship of the orifice plate, which was obtained though calibration. Fig. 3 presents a view of the model with the measuring equipment installed.

In these tests, two model configurations were considered, each one with a different variable ballast mass. Therefore, for each configuration, the buoy presented distinct draft, mass and mass distribution. The characteristics of each configuration are presented in Table 1. The same mooring system was used for both configurations. It consists of three lines (ML1, ML2, ML3), made from six strand steel wire, equally spaced in the tangential direction around a vertical axis located at the centre of the buoy in still water conditions, as shown in Fig. 4. Each line connecting the buoy fairlead to the floor was divided into three segments (with lengths L_1, L_2 and L_3), with a clump weight and a jumper (or riser) at the connections of the segments, as shown in Fig. 5. Such a mooring concept is popular in wave energy applications [38], since it is able to keep the device in station while having little influence on the response in the DoF in which energy is extracted [39]. Through the control of the mass and density of the clump weight and jumper, it is possible to control the stiffness and pretension of the mooring system [40]. Relevant full-scale parameters of the mooring system are presented in Table 2.

Table 1
Physical characteristics of the Spar-buoy OWC model, for the two mass distributions considered.

Parameter	Config. D1	Config. D2
Buoy diameter, d_1 [m]	16.00	16.00
OWC diameter, d_2 [m]	5.89	5.89
Total length [m]	64.06	64.06
Floater section draft l_1 [m]	6.17	7.91
Buoy draft, l_t [m]	49.17	50.91
Air chamber height, l_c [m]	14.89	13.15
z-coordinate of CoB, z_B [m]	− 22.99	− 22.24
z-coordinate of CoG, z_G [m]	− 28.50	− 31.96
Metacentric height, $\overline{GM}_0$ [m]	6.73	10.81
Displaced volume, V [m^3]	2.5986×10^3	2.9013×10^3
Buoy mass, m [kg]	2.6027×10^6	2.9140×10^6
Mom. inertia around x-axis at CoG, I_{xx} [kg m^2]	1.4437×10^9	1.5310×10^9
Mom. inertia around z-axis at CoG, I_{zz} [kg m^2]	0.1002×10^9	0.1118×10^9

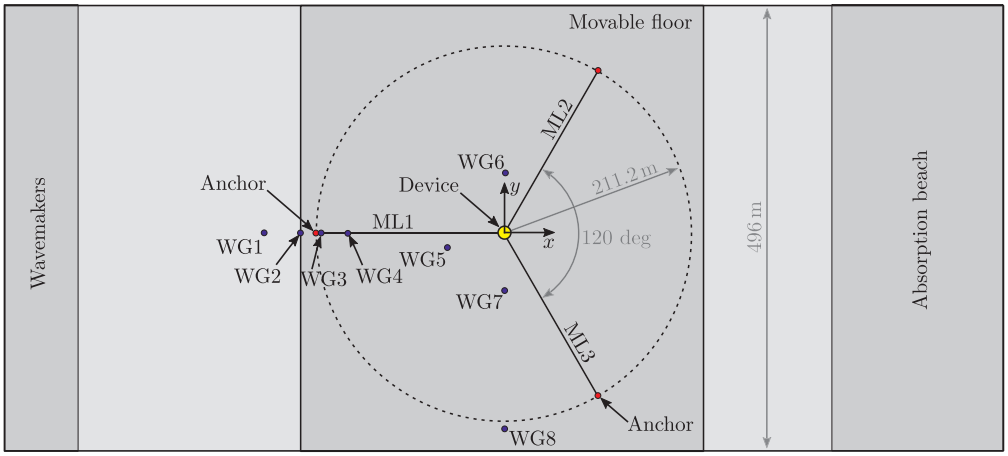

Fig. 4. Schematic representation of the ocean basin, model position, mooring lines (ML1, ML2, ML3) and wave gauges (WG4, WG6, WG8). The dimensions presented refer to full scale.

4. Numerical model

The leading criteria for the definition of a numerical model is the definition of an appropriate compromise of accuracy and computational time [41], compatible with the specific application the model is intended to serve [42]. The objective of this paper is to produce and validate a numerical simulation tool to inform and guide the design of the floater, the air turbine configuration, and the mooring system. Therefore, medium–high speed of computation is a mandatory requirement in order to investigate a wide variety of wave conditions and device configurations. However, a major objective is to detect parametric resonance, which was found to be detrimental for power extraction [17] and potentially threatening the floater and mooring survivability [43]. Since parametric instabilities are due to time-varying parameters of the system [1], nonlinear models are required. However, fully-nonlinear models, either based on computational fluid dynamics (CFD) [44] or on potential flow [45], as well as weakly-nonlinear potential flow models [46], although virtually able to articulate parametric resonance, are too computationally expensive for extensive design applications.

Partially-nonlinear potential flow models are a more parsimonious option, since only the most important nonlinearities are implemented. In particular, for the device considered in this paper, it is possible to assume linear radiation and diffraction forces, since the characteristic wavelengths are much larger than the horizontal dimension of the device, and its dynamics are governed by Froude-Krylov forces [47]. Nonlinear Froude-Krylov models have been implemented in the literature, showing good agreement with experimental data and confirming the ability to detect parametric resonance for spar-like WECs [48]. However, such models describe the wetted surface through panel-discretization, hence implementing computationally-expensive re-meshing routines, hindering their application for extensive design studies. Nevertheless, a more computationally-efficient approach was recently developed [49], which exploits the axisymmetric assumption to provide an analytical representation of the wetted surface. This model was shown to be able to articulate parametric resonance of a simplified Spar-buoy-like device, both in regular [50] and irregular [51] waves. The present paper purports to validate this modelling approach by comparison with experimental data, described in Section 3. The detailed description of the numerical model is provided in the following sections.

Table 2
Mooring system parameters at full scale, considering the different locations of the fairlead for configurations D1 and D2.

Parameter	Value
Line diameter, d_L [mm]	32
Net line linear density, w_L [kg m^{-1}]	34.82
Jumper mass, m_J [kg]	4030.46
Jumper density, ρ_J [kg m^{-3}]	123.00
Clump-weight mass, m_C [kg]	36139.83
Clump-weight density, ρ_C [kg m^{-3}]	8097.50
Length of line anchor-jumper, L_1 [m]	143.28
Length of line jumper-clump-weight, L_2 [m]	37.01
Length of line fairlead-clump-weight, L_3 [m]	50.40
Anchor radius, r_A [m]	211.2
Anchor z-coordinate, z_A [m]	−80
Fairlead radial coordinate, r_F [m]	9.28
Fairlead z-coordinate (config. D1), $z_{F,1}$ [m]	−0.82
Fairlead z-coordinate (config. D2), $z_{F,2}$ [m]	−2.58

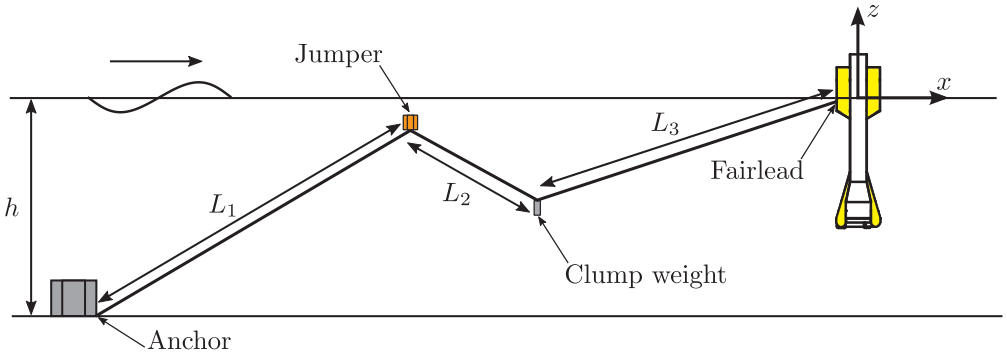

Fig. 5. Schematic representation of a single mooring line and connection to the buoy and to the tank floor.

4.1. Hydrodynamic model

Linear potential flow theory can be applied by assuming inviscid, irrotational and incompressible fluid motion. Under such conditions, a boundary element method (BEM) software can be used to compute hydrodynamic characteristics of the floater, namely added mass, radiation damping, Froude-Krylov force, and diffraction force. The commercial software WAMIT [52] is preferred, since it better handles problems with thin elements and moonpools [53]. WAMIT is a panel method code that applies Green's theorem to derive velocity potentials on a spatial distribution of singularities over the wetted surface of the floater under the still water level (SWL). In WAMIT, apart from standard source-type singularities, dipole-type singularities can be used to better describe zero-thickness regions of the floater. Furthermore, a higher-order method can be used to represent the velocity potential in a continuous fashion by means of B-splines [28]. The irregular-frequency problem affecting the velocity potential, which normally occurs in free-surface piercing bodies, is removed by closing the inner floater volume at the free surface.

The device is considered as a two-body system composed of the floater (first body) and of the water column enclosed by the floater (second body), which moves along the OWC tube. In particular, the top part of the water column is treated as a heaving rigid cylindrical piston, with cross sectional area equal to the moonpool area, and of finite height (5 m), as suggested in [28]. Therefore, there are seven degrees of freedom (DoFs), six of the floater, and the 7th of the water piston. The hydrodynamic parameters are computed around a point on the symmetry axis of the system and at the SWL. Fig. 6 shows the resulting added mass and radiation damping curves, for configuration D2, in all significant DoFs (off-diagonal terms are symmetric and, due to symmetry, sway and roll are equal to surge and pitch, respectively, while yaw is null). Froude-Krylov force curves are presented in Fig. 10 in Section 4.2.1. Hydrodynamic coefficients for configuration D1 are similar to D2, since the main difference is the mass distribution.

Although WAMIT returns parameters in the frequency domain, the equation of motion should be written in the time domain in order to include nonlinearities. Thanks to Ogilvie's relationship [54], radiation effects can be computed, in time domain, through direct computation of the convolution integral of the radiation impulse response function. Alternatively, a more computationally convenient approach is to implement a state space approximation of the convolution integral, obtained through a finite-order identification by moment-matching [55].

A 2nd-order Runge–Kutta time-integration scheme is used to determine the response of the system. The constant time step is used, achieving a satisfactory compromise between accuracy and computational time. Convergence is studied by considering the response amplitude operator (RAO) in linear conditions, i.e. with a small wave and a fictitious linear mooring stiffness, and with zero PTO damping. The RAO is reconstructed, in time domain, by considering a wide range of regular waves with period T_w, and constant wave height, $H_w = 0.02$ m. The time step (Δt) is chosen to be $T_w/50$. Furthermore, in order to verify the correctness of implementation, the accuracy of the radiation approximation, and the convergence of the time step, the resulting response is compared to the RAO computed through the frequency domain curves from WAMIT, as shown in Fig. 7 for configuration D2.

4.2. Equation of motion

As discussed in Section 4.1, a 7-DoF system has to be defined, which is obtained by adding the OWC displacement to the 6 DoFs of the floater. In this section, for sake of clarity and generality, the 6-DoF dynamics of the floater are first presented. It is then straightforward to expand the system to 7 DoFs, since the coupling between the floater and the OWC happens mainly through the power take-off system (turbine and air chamber) and, to a lesser extent, through wave radiation and viscous damping.

The dynamics and kinematics of the floater are conveniently represented by two right-handed frames of reference, as schematically shown in Fig. 8 for a generic axisymmetric device. The first frame (x, y, z) is inertial (world-fixed), with the x-axis along and in the same positive direction of the wave propagation, the z-axis pointing upwards, and with the origin at the still water level and lying on the axis of the buoy at rest. The inertial frame is used to describe the body displacements ($\boldsymbol{\zeta}$), divided into translations ($\mathbf{p}$) and rotations ($\boldsymbol{\Theta}$):

$$\boldsymbol{\zeta} = \begin{bmatrix} \mathbf{p} \\ \boldsymbol{\Theta} \end{bmatrix} \quad , \quad \mathbf{p} = \begin{bmatrix} x \\ y \\ z \end{bmatrix} \quad , \quad \boldsymbol{\Theta} = \begin{bmatrix} \phi \\ \theta \\ \psi \end{bmatrix}, \tag{6}$$

where x is surge, y is sway, z is heave, ϕ is roll, θ is pitch, and ψ is yaw.

The second right-handed frame of reference is $(\hat{x}, \hat{y}, \hat{z})$, fixed with the body, hence non-inertial, and initially overlapping with the inertial frame when the buoy is at rest. The body-fixed frame is convenient for writing the dynamic equation of the system, since the inertial properties remain constant in time. Therefore, both forces and velocities are

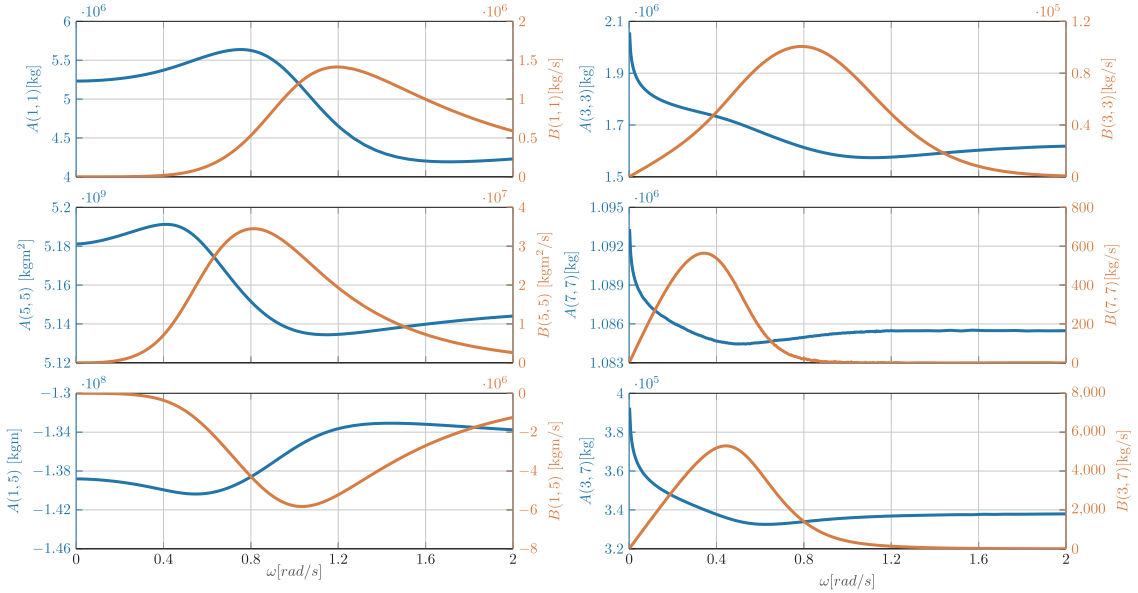

Fig. 6. Added mass (A) and radiation damping (B) coefficients as a function of the wave frequency for configuration D2.

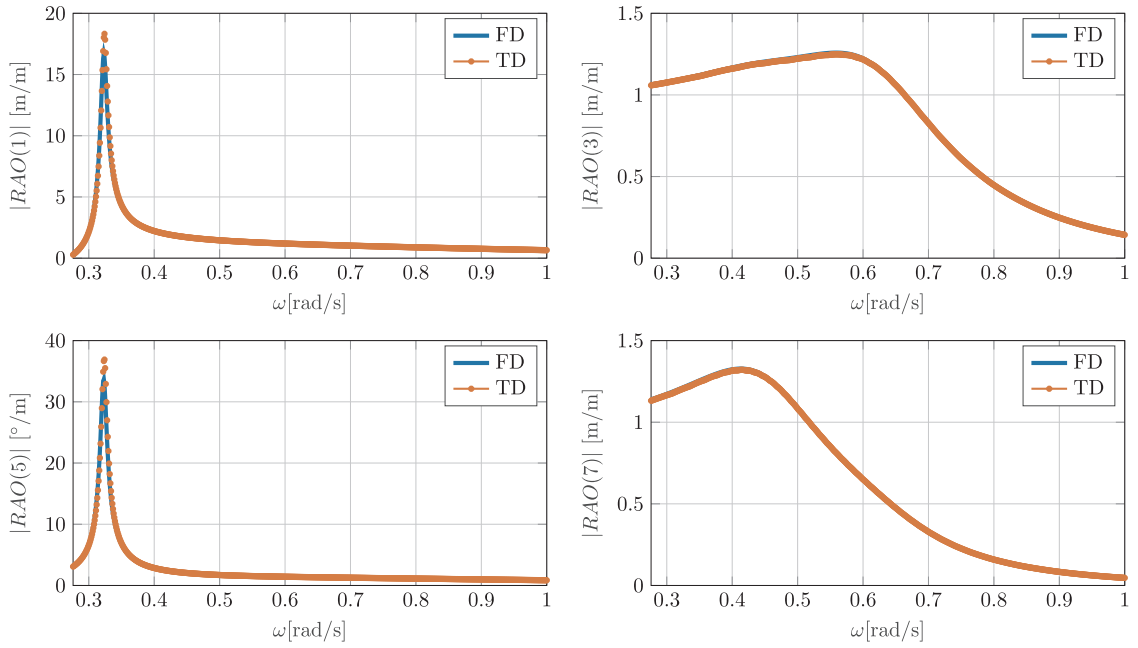

Fig. 7. Magnitude of the response amplitude operator (RAO) for configuration D2, under linear conditions (wave amplitude of 0.01 m and linearized mooring forces) and with no power take-off damping, computed using a frequency domain (FD) data and a time domain (TD) model with a time step equal to $\frac{1}{50}\frac{2\pi}{\omega}$.

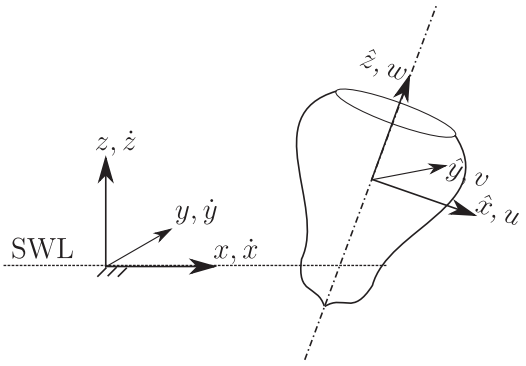

Fig. 8. Inertial frame (x, y, z), with the origin at still water level (SWL), and body-fixed (non-inertial) frame $(\hat{x}, \hat{y}, \hat{z})$, after an arbitrary displacement. At rest the two frames coincide. Velocities according to the inertial frame $(\dot{x}, \dot{y}, \dot{z})$ and the body-fixed frame (u, v, w).

represented in the body-fixed frame, along the axis of the buoy. Velocities ($\boldsymbol{\nu}$), divided into translation ($\mathbf{v}$) and rotations ($\boldsymbol{\omega}$), are defined as:

$$\boldsymbol{\nu} = \begin{bmatrix} \mathbf{v} \\ \boldsymbol{\omega} \end{bmatrix} \quad , \quad \mathbf{v} = \begin{bmatrix} u \\ v \\ w \end{bmatrix} = \begin{bmatrix} \dot{\hat{x}} \\ \dot{\hat{y}} \\ \dot{\hat{z}} \end{bmatrix} \quad , \quad \boldsymbol{\omega} = \begin{bmatrix} p \\ q \\ r \end{bmatrix}. \tag{7}$$

It is worth remarking that forces and velocities are along time-varying axes, while displacements are along fixed axes. In linear hydrodynamic models there is no difference between such axes, based on the assumption of small displacements. However, in a nonlinear approach, a mapping from body- to world-frame velocities should be applied, at each time step, in order to obtain the correct displacements. One possible mapping is the following:

$$\dot{\boldsymbol{\zeta}} = \begin{bmatrix} \dot{\mathbf{p}} \\ \dot{\boldsymbol{\Theta}} \end{bmatrix} = \begin{bmatrix} \mathbf{R}_{\boldsymbol{\Theta}} & \mathbf{0}_{3\times3} \\ \mathbf{0}_{3\times3} & \mathbf{T}_{\boldsymbol{\Theta}} \end{bmatrix} \begin{bmatrix} \mathbf{v} \\ \boldsymbol{\omega} \end{bmatrix} = \mathbf{J}_{\boldsymbol{\Theta}}\boldsymbol{\nu}, \tag{8}$$

where $\mathbf{R}_{\boldsymbol{\Theta}}$ is the rotation matrix, depending on the Euler angles $\boldsymbol{\Theta}$, defined according to the 3–2-1 convention as:

$$\mathbf{R}_{\boldsymbol{\Theta}} = \mathbf{R}_{\hat{z},\psi}\mathbf{R}_{\hat{y},\theta}\mathbf{R}_{\hat{x},\phi} = \begin{bmatrix} c\psi & -s\psi & 0 \\ s\psi & c\psi & 0 \\ 0 & 0 & 1 \end{bmatrix} \begin{bmatrix} c\theta & 0 & s\theta \\ 0 & 1 & 0 \\ -s\theta & 0 & c\theta \end{bmatrix} \begin{bmatrix} 1 & 0 & 0 \\ 0 & c\phi & -s\phi \\ 0 & s\phi & c\phi \end{bmatrix},$$

with c and s standing for cos() and sin() trigonometric operators, respectively. $\mathbf{R}_{\boldsymbol{\Theta}}$ is applied to translational velocities. $\mathbf{T}_{\boldsymbol{\Theta}}$ is applied to rotational ones, and is defined as follows:

$$\mathbf{T}_{\boldsymbol{\Theta}} = \begin{bmatrix} 1 & s\phi t\theta & c\phi t\theta \\ 0 & c\phi & -s\phi \\ 0 & s\phi/c\theta & c\phi/c\theta \end{bmatrix}, \tag{9}$$

where t stands for the tan() trigonometric operator. Note that the singularity of $\mathbf{T}_{\boldsymbol{\Theta}}$ in $\pm\pi/2$ is usually not an issue in wave energy applications, since the amplitude of the pitch angle is, by design, always expected to be smaller than $\pi/2$.

Another consequence of using a body-fixed frame are Coriolis and centripetal forces, which are normally neglected under the assumption of small rotational velocities. Let us define, for convenience of notation, the skew-symmetric operator $\mathscr{S}$: $\mathbb{R}^3 \rightarrow \mathbb{R}^{3\times3}$ as

$$\mathscr{S}: \left\{ \boldsymbol{\lambda} \in \mathbb{R}^3 \;\middle|\; \mathscr{S}(\boldsymbol{\lambda}) \triangleq \begin{bmatrix} 0 & -\lambda_3 & \lambda_2 \\ \lambda_3 & 0 & -\lambda_1 \\ -\lambda_2 & \lambda_1 & 0 \end{bmatrix} \right\}. \tag{10}$$

It follows that $\mathscr{S}(\boldsymbol{\lambda}) = -\mathscr{S}(\boldsymbol{\lambda})^T$, and that the cross-product can be written as:

$$\boldsymbol{\lambda} \times \mathbf{a} = \mathscr{S}(\boldsymbol{\lambda})\mathbf{a} \tag{11}$$

Using such a notation, it is possible to define Coriolis and centripetal forces as [56]:

$$\mathbf{F}_{Cor} = \mathbf{C}_{Cor}\boldsymbol{\nu} = \begin{bmatrix} M\mathscr{S}(\boldsymbol{\omega}) & -M\mathscr{S}(\boldsymbol{\omega})\mathscr{S}(\mathbf{r_g}) \\ M\mathscr{S}(\mathbf{r_g})\mathscr{S}(\boldsymbol{\omega}) & -\mathscr{S}(\mathbf{I}_r\boldsymbol{\omega}) \end{bmatrix} \begin{bmatrix} \mathbf{v} \\ \boldsymbol{\omega} \end{bmatrix}, \tag{12}$$

where M is the mass of the body, $\mathbf{r}_g$ is the vector from the origin of the body-fixed frame (reference point) to the centre of gravity, and $\mathbf{I}_r$ is the matrix of the moments of inertia with respect to the reference point.

Finally, the dynamical equation in 6 DoFs for the floater becomes:

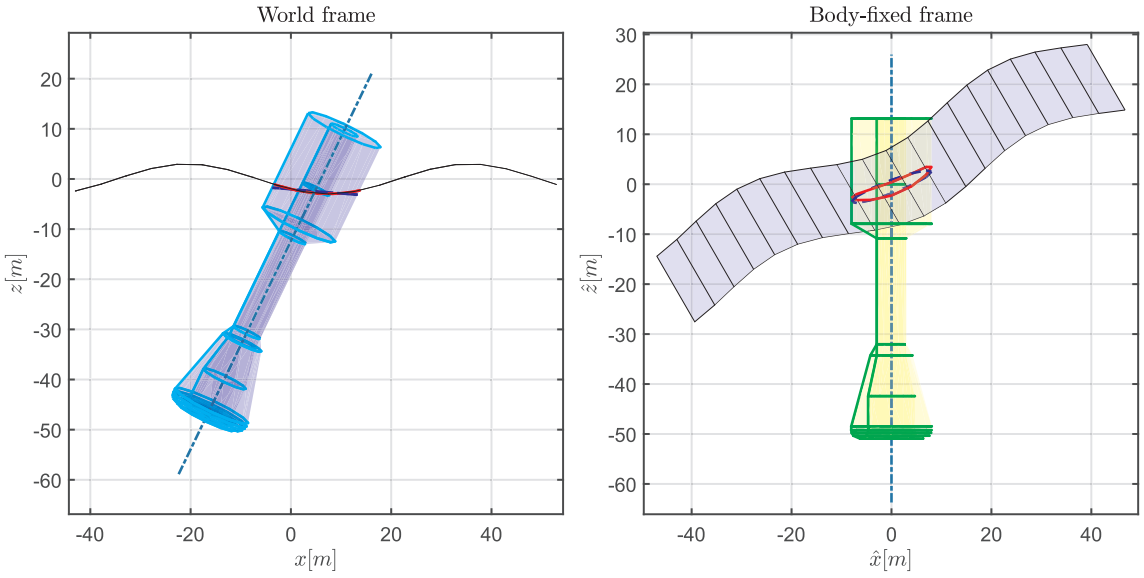

Fig. 9. Example of displaced buoy D2, in the world frame (on the left) and body-fixed frame (on the right), with corresponding mapped wave field and its intersection with the buoy.

$$\begin{cases} \dot{\boldsymbol{\zeta}} = \mathbf{J}_{\boldsymbol{\Theta}}\boldsymbol{\nu} \\ \mathbf{M}\dot{\boldsymbol{\nu}} + \mathbf{C}_{Cor}\boldsymbol{\nu} = \sum_i \mathbf{F}_i \end{cases} \tag{13}$$

where $\mathbf{M}$ is the inertial matrix and $\mathbf{F}_i$ comprises all external forces, namely diffraction, Froude-Krylov, radiation, drag, power take-off, and mooring loads. Note that $\mathbf{F} \in \mathbb{R}^6$ is a generalized force, composed of a linear force vector $\mathbf{f} \in \mathbb{R}^3$, and a torque vector $\boldsymbol{\tau} \in \mathbb{R}^3$. While radiation and diffraction can be assumed as linear, a nonlinear representation of FK forces, viscous drag effects, PTO force, and mooring loads is implemented, as further explained in Sections 4.2.1, 4.2.2, 4.2.3, and 4.2.4, respectively. Finally, note that the 6-DoF dynamic system in (13) for the floater is readily expanded to 7-DoFs by appending the water column velocity to $\boldsymbol{\nu}$ and expanding $\mathbf{M}$, $\mathbf{J}_{\boldsymbol{\Theta}}$, $\mathbf{C}_{Cor}$, and $\mathbf{F}$ accordingly.

4.2.1. Nonlinear Froude-Krylov force

Froude-Krylov forces are defined as the integral of the undisturbed pressure field (P) over the wetted surface of the floater. In the linear approximation, it is assumed that the relative motion between the body and the free surface is small, so that FK forces are computed with respect to the mean wetted surface. On the contrary, nonlinear FK force calculations are performed with respect to the actual *instantaneous* wetted surface ($S_w(t)$):

$$\mathbf{f}_{FK} = \mathbf{f}_g + \iint_{S_w(t)} P\mathbf{n}\, dS, \tag{14a}$$

$$\boldsymbol{\tau}_{FK} = \mathbf{r}_g \times \mathbf{f}_g + \iint_{S_w(t)} P\mathbf{r} \times \mathbf{n}\, dS, \tag{14b}$$

where $\mathbf{f}_g$ is the gravity force, $\mathbf{n}$ is the unity vector normal to the surface, $\mathbf{r}$ is the generic position vector, and $\mathbf{r}_g$ is the position vector of the centre of gravity. The undisturbed incident pressure field of an unidirectional regular wave is defined as:

$$P\left(x, z, t\right) = -\rho g z + a\cos(\omega t - kx)\frac{\cosh(k(z'+h))}{\cosh(kh)}, \tag{15}$$

where a, ω, and k are the wave amplitude, frequency, and wavenumber, respectively, ρ the water density, g the acceleration of gravity, h the water depth, and z' the vertical coordinate modified according to Wheeler's stretching [57].

Solving the integrals in (14) requires, in general, computationally demanding mesh-based approaches. However, computationally efficient approaches are available for axisymmetric bodies [42], exploiting cylindrical coordinates (ϱ, ϑ) to achieve an analytical representation of the wetted surface:

$$\begin{cases} \hat{x}(\varrho, \vartheta) = f(\varrho)\cos\vartheta \\ \hat{y}(\varrho, \vartheta) = f(\varrho)\sin\vartheta, \\ \hat{z}(\varrho, \vartheta) = \varrho \end{cases} \quad \vartheta \in \left[-\pi, \pi\right) \wedge \varrho \in \left[\varrho_1, \varrho_2\right] \tag{16}$$

where $f(\varrho)$ is a generic function of the vertical coordinate ϱ, describing the profile of revolution of the axisymmetric body. Since it is convenient to define the FK integrals in the body-fixed frame of reference, the pressure field must be mapped from the global to the body-fixed frame. Moreover, note that describing the FK integrals in the body-frame also reduces the number of integrals to be computed, since cylindrical sections have horizontal normals (the integral in heave is zero), and disks sections have vertical normals (integrals in surge and sway are null) [49]. After some manipulations [42], the integral in (14a), for example, becomes:

$$\begin{aligned} \mathbf{f}_{FK} &= \mathbf{R}_{\boldsymbol{\Theta}}^T\mathbf{f}_g + \iint_{S_w(t)} P\left(\hat{x}, \hat{y}, \hat{z}\right)\mathbf{n}\, dS \\ &= \mathbf{R}_{\boldsymbol{\Theta}}^T\mathbf{f}_g + \int_{-\pi}^{\pi}\int_{\varrho_1}^{\varrho_2} P\left(\varrho, \vartheta\right)(\mathbf{e}_\varrho \times \mathbf{e}_\vartheta)\, d\varrho\, d\vartheta, \end{aligned} \tag{17}$$

where $\mathbf{e}_\varrho$ and $\mathbf{e}_\vartheta$ are the unit vector along ϱ and ϑ, respectively. Note that when internal patches (facing the water column) are considered, the sign of the normal vector in (17) should be reversed. The integral in (17) is solved numerically, using a 2D-quadrature scheme for trapezoidal integration [58]. An open source Matlab demonstration toolbox for definition and computation of nonlinear FK forces for axisymmetric floaters is available at [59].

Fig. 9 shows, for an arbitrary displacement of the buoy and wave field, the configuration in both the world-frame (on the left) and the body-frame (on the right), and the corresponding mapping of the free surface elevation. Note that the mesh-like representation in Fig. 9 has a mere visualization purpose, since the surfaces are described analytically and no mesh is needed.

Note that the considered geometry is rather complex, with several changes of cross-sectional area. Twelve different patches can be identified, namely 5 cylindrical sections, 4 conical sections, 2 quarters of torus, and a disk for the inner piston. This increases the overall computational time, since each patch requires an independent formulation, hence raising the number of integrals to be computed. However, it is

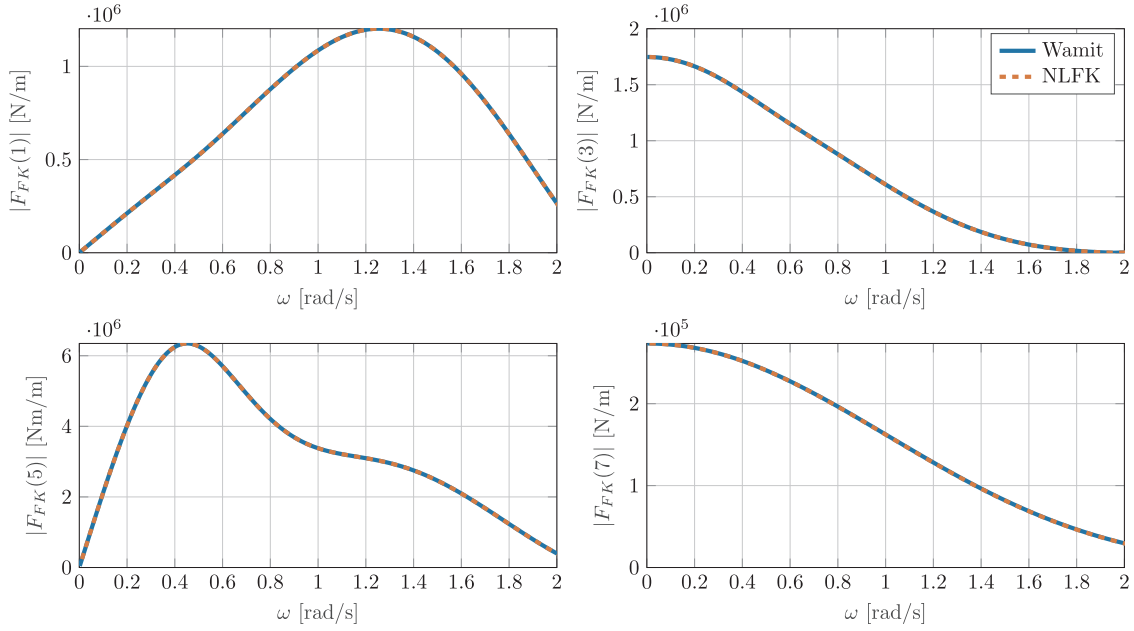

Fig. 10. Froude-Krylov force coefficients as a function of the wave frequency for configuration D2, computed via linear (WAMIT) and nonlinear (NLFK) models, under small wave-amplitude conditions (0.01 m wave amplitude and fixed floater).

worth remarking that equally considering all patches is likely to be unnecessary, since some patches are relatively small and/or so deep that the dynamic pressure has already significantly decayed. Nevertheless, since the purpose of this paper is validation rather than computational time minimization, no simplifying assumption has been investigated.

Finally, in order to verify the correctness of the implementation of the NLFK integrals and mapping functions, as well as validating the modelling approach, it is possible to compare linear and nonlinear FK forces calculations under linear conditions. In fact, considering no displacement and a very small wave amplitude (0.01 m), both linear and nonlinear forces must agree, as shown in Fig. 10.

4.2.2. Viscous drag force

In un-damped systems, meeting the frequency condition is sufficient for the arise of parametric resonance. Conversely, in real applications, an additional necessary condition for the appearance of parametric instability is that the internal parametric excitation exceeds the damping of the system. Likewise, the severity of the parametric response is a direct consequence of dissipative effects. Therefore, an appropriate modelling of viscous effects is essential for studying parametric resonance.

In potential flow-based nonlinear models, viscous drag forces are commonly included by means of a Morison-like term, which suggests a quadratic dependence of the drag force on the relative velocity between the body and the fluid. Given a variable cross sectional area and since the total length of Spar-buoy OWC device is comparable to the decay rate of the fluid velocity with water depth, it is convenient to implement an integral approach to the Morison-like equation [32]. In particular, the viscous force ($\mathbf{F}_{vis}$) is defined for an infinitesimal cross sectional area of the buoy, perpendicular to $\hat{z}$, and then integrated over the whole length. The cylindrical coordinates of the nonlinear Froude-Krylov framework, described in Section 4.2.1, can be used to compute such integrals, applying a similar mapping of the fluid velocity from the world frame to the body-fixed frame.

For surge and sway DoFs, drag forces result in:

$$\mathbf{F}_{vis}(1) = -\frac{1}{2}\rho C_{d,c} \int_{\varrho_1}^{\varrho_2} 2f(\varrho) u_r \left| u_r \right| \, d\varrho, \tag{18a}$$

$$\mathbf{F}_{vis}(2) = -\frac{1}{2}\rho C_{d,c} \int_{\varrho_1}^{\varrho_2} 2f(\varrho) v_r \left| v_r \right| \, d\varrho, \tag{18b}$$

where $C_{d,c}$ is the drag coefficient around a circular cylinder, u_r and v_r are the horizontal relative velocities along $\hat{x}$ and $\hat{z}$, respectively. Note that, as shown in (16), $2f(\varrho)$ represents the function describing the buoy diameter variation with depth.

The infinitesimal viscous force contribution in (18) also generates a viscous torque, acting in roll and pitch:

$$\mathbf{F}_{vis}(4) = \frac{1}{2}\rho C_{d,c} \int_{\varrho_1}^{\varrho_2} 2f(\varrho) v_r \left| v_r \right| \varrho \, d\varrho, \tag{19a}$$

$$\mathbf{F}_{vis}(5) = -\frac{1}{2}\rho C_{d,c} \int_{\varrho_1}^{\varrho_2} 2f(\varrho) u_r \left| u_r \right| \varrho \, d\varrho. \tag{19b}$$

The drag torque in yaw is assumed to be dependent only on the buoy rotation ($r = \omega(3)$) and is caused by the friction with the surrounding fluid, quantified by the drag coefficient $C_{d,6}$. Considering the linear velocity of a point on the external surface equal to the rotational velocity times the distance from the axis, yaw component of the viscous force becomes:

$$\mathbf{F}_{vis}(6) = -\pi\rho C_{d,6} \int_{\varrho_1}^{\varrho_2} f(\varrho)^4 r \left| r \right| \, d\varrho. \tag{20}$$

Finally, drag forces in heave due to the interaction with the external wave field and the friction with the water column ($F_{3,7}$) are:

$$F_{3,7} = -\frac{1}{2}\rho C_{d,37} A_p (\hat{\dot{z}} - \hat{\dot{z}}_7)|\hat{\dot{z}} - \hat{\dot{z}}_7|, \tag{21a}$$

$$\mathbf{F}_{vis}(3) = F_{3,7} - \frac{\pi}{2}\rho C_{d,3} \int_{\varrho_1}^{\varrho_2} f(\varrho)^2 w_r \left| w_r \right| \, d\varrho, \tag{21b}$$

where A_p is the cross sectional area of the water piston, $C_{d,3}$ the drag coefficient in heave, and w_r is the relative heave velocity of the buoy with respect to the fluid. Note that $F_{3,7}$ acts on the water column as a reaction force, hence with opposite sign.

The drag coefficients ($C_{d,c}$, $C_{d,3}$, $C_{d,37}$, and $C_{d,6}$) can be chosen as the ones minimizing the error between the numerical model and a higher-fidelity benchmark, either using CFD simulations or experimental data. In this work, a sensitivity analysis of the simulated response to different

combinations of drag coefficients has been performed and most significant results are discussed in Section 5.

4.2.3. Power take-off force

The power take-off system of an OWC is an air turbine, which converts the bidirectional air flow induced by the OWC motion inside the floater. The pressure drop across the turbine can be simulated at model scale using an orifice plate [60].

The effect of air compressibility inside the chamber has been neglected since, while it introduces a phase lag between the water column and the floater motion, affecting power conversion, it usually does not have a significant impact on the hydrodynamic response of the floater, especially in rotational DoFs. However, note that air compressibility effects are negligible at small scale testing but not at full-scale. Therefore, under normal operation, the interaction between the water piston and the floater occurs due to the pressure variations inside the air chamber, which in turn depends on the relative displacements and on the diameter of the orifice plate [32]:

$$F_{PTO} = \frac{8\rho_a A_a^3}{\pi^2 C_d^2 d_0^4}(\hat{\dot{z}} - \hat{\dot{z}}_7)|\hat{\dot{z}} - \hat{\dot{z}}_7| \tag{22}$$

where ρ_a is the air density, A_a is the cross-sectional area of the air chamber (equal to A_p), C_d is the discharge coefficient ($C_d = 0.6466$ for the orifice plate used in the experiments), d_0 is the diameter of the orifice plate, and $\hat{\dot{z}}_7$ is the velocity of the water column along the axis of the buoy. Note that F_{PTO} acts on both the buoy and the water column, but with opposite sign.

4.2.4. Mooring force

The mooring system, schematically shown in Fig. 11, is based on the experimental tests performed at the ocean basin of the University of Plymouth (UK) [13]. It is composed of three lines equally spaced in the circumferential direction relative to the buoy axis of symmetry at rest. Each line is divided in ulterior three segments, connecting the anchor to a jumper (line of length L_1), then to a clump weight (line of length L_2), and finally to the buoy (line of length L_3), as depicted in Fig. 5. Such a mooring concept is popular in wave energy applications, since it is able to keep the device in station while having little influence on the response in the DoF were energy is extracted [39]. For this application, the mass and density of the jumper (or riser) and the clump weight were chosen to match the desired stiffness of the mooring system. Relevant parameters for the equivalent full-scale model of the mooring system are tabulated in Table 2.

A quasi-static model is defined to compute the tension on each line depending on the 6-DoFs displacements of the attachment points of the buoy and consequently obtain the total forces and torques acting on the floater, around the origin of the body-fixed frame and along its axes. Relying on the fact that for this system each line is always tensioned and they have a relatively small mass, it is possible to treat each mooring line as always straight. The problem can be simplified as two-dimensional, by defining each mooring line on a vertical plane containing the buoy fairlead and the anchor point. For each line, the positions of each component can be represented by the horizontal coordinate r and the vertical coordinate z, considering the origin of the referential at the anchor point. Consequently, for each line, two equations are written for the vertical and horizontal force equilibrium (Eqs. (23) and (24), respectively), one for the torque balance (Eq. (25)), and two for imposing geometrical constraints (Eqs. (26) and (27)):

$$T_F \sin\Phi_3 - w_L(L_1 + L_2 + L_3) - F_C + F_J - T_A \cos\Phi_1 = 0 \tag{23}$$

$$T_F \cos\Phi_3 - T_A \cos\Phi_1 = 0 \tag{24}$$

$$T_F \cos\Phi_3 z_F - T_F \sin\Phi_3 r_F + w_L(L_1 r_1 + L_2 r_2 + L_3 r_3) + F_C r_C - F_J r_J = 0 \tag{25}$$

$$L_1 \cos\Phi_1 + L_2 \cos\Phi_2 + L_3 \cos\Phi_3 - r_F = 0 \tag{26}$$

$$L_1 \sin\Phi_1 - L_2 \sin\Phi_2 + L_3 \sin\Phi_3 - z_F = 0 \tag{27}$$

where r_F and z_F are the horizontal and vertical distances between the buoy fairlead and the anchor, respectively, while F_C and F_J are the net force of the clump weight and jumper, respectively, obtained as the balance between their weight and buoyancy. The horizontal distance of the midpoint of line L_i to the anchor is r_i, for $i \in [1, 2, 3]$, while r_C and r_J are the horizontal distances of the jumper and clump weight from the anchor, respectively. The variable w_L represents the line submerged weight per unit length. Such parameters are simple linear combinations of the five unknowns of the system, which are: tension at the buoy fairlead (T_F), tension at the anchor (T_A), and angles of each line to the horizontal direction (Φ_1, Φ_2, Φ_3), as shown in Fig. 11. Knowing the tension and the angles of each line, it is possible to compute the total force and total torque acting on the buoy. Note that the nonlinear system of equations in Eqs. (23)–(27) is solved numerically, since no explicit algebraic solution can be obtained.

5. Results

In order to give a closure to the numerical model described in

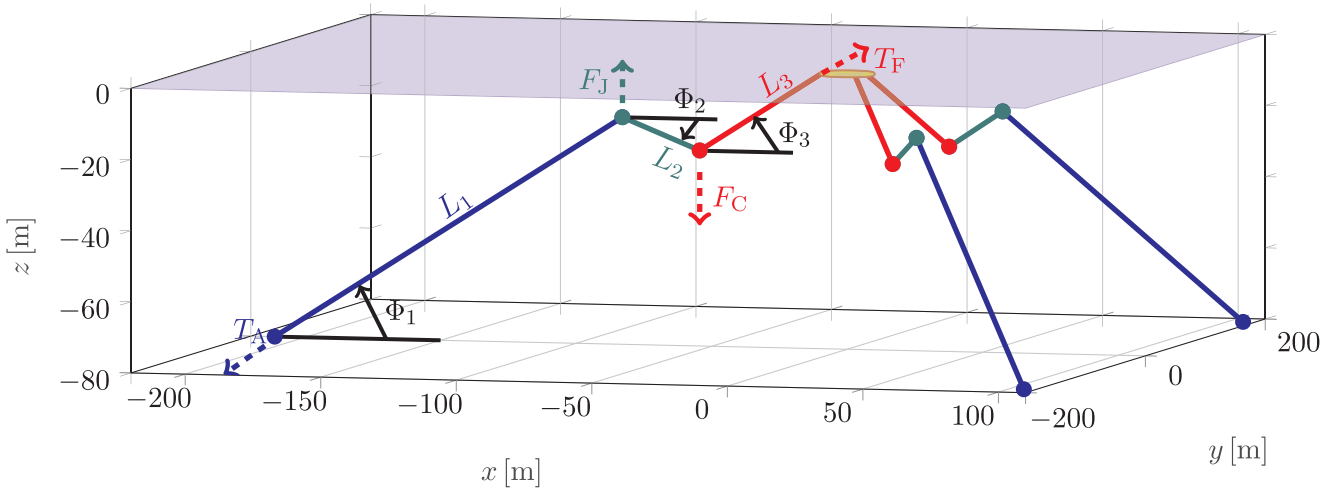

Fig. 11. Mooring system layout with three lines separated tangentially with an angle of 120°. Each line is divided in three segments of length L_1, L_2, and L_3. F_C is the net clump-weight force and F_J is the net jumper force (negative in the figure). The quasi-static model solves for the tension at the buoy fairlead (T_F), the tension at the anchor (T_A), and the angles of the three lines (Φ_1, Φ_1, and Φ_3).

Table 3
Significant set of drag coefficients used to produce results in Section 5.1. The best configuration is for a relative error metric ($\Pi_i/\Pi_{i,\min}$) of 1.

$C_{d,c}$	$C_{d,3}$	$C_{d,37}$	$C_{d,6}$	$\Pi_i/\Pi_{i,\min}$
2	0.175	0.2	0.1	1.0837
1.75	**0.175**	**0.2**	**0.1**	**1.0000**
2	0.15	0.2	0.1	1.0104
1.75	0.15	0.2	0.1	1.0866
2	0.175	0.2	0.125	1.1217
1.75	0.175	0.2	0.125	1.0211
2	0.15	0.2	0.125	1.0387
1.75	0.15	0.2	0.125	1.1265

Section 4, a set of drag coefficients should be identified. Moreover, an appropriate description of dissipation mechanisms is important in the study of parametric resonance, since viscous effects can hinder the full development of the parametric resonance. All results in Section 5 are presented for the set of all possible combinations of 2 values for each one of the 4 drag coefficients ($C_{d,c}$, $C_{d,3}$, $C_{d,37}$, $C_{d,6}$), as shown in Table 3, for a total of 16 combinations. However, note that, for sake of clarity, Table 3 presents the most representative subset of a wider range of drag coefficients that has been considered in the sensitivity analysis.

For each drag coefficient configuration (i), an accuracy metric (Π_i) has been defined in order to provide a global measurement of goodness of fit over the whole range of waves considered and all DoFs. In each wave (n_w) and DoF (j), the relative error ($\varpi_j^{n_w}$) has been defined as the difference between the amplitude predicted by the experimental measurement (computed as $RMS(\zeta_e(j) - \overline{\zeta_e(j)})$) and the mathematical model (computed as $RMS(\zeta_m(j) - \overline{\zeta_m(j)})$), normalized by the maximum amplitude registered in the experiments for that DoF:

$$\varpi_j^{n_w} = \left[\frac{RMS(\zeta_e(j) - \overline{\zeta_e(j)}) - RMS(\zeta_m(j) - \overline{\zeta_m(j)})}{\max_i \left(RMS\left(\zeta_e(j) - \overline{\zeta_e(j)} \right) \right)} \right]_{n_w} \tag{28}$$

Consequently, for each configuration i, Π_i is defined as the mean of all $\varpi_j^{n_w}$, so that the best configuration of drag coefficients is the one with the lowest Π.

Table 3 presents the ratio between each Π_i and the minimum value found in those simulations ($\Pi_{i,\min}$), highlighting in bold the best combination of drag coefficients. Since the motion of the floater is found not to be significantly sensitive to the damping, due to viscous flow effects, between the moonpool and the water column, only one $C_{d,37}$ value is reported in Table 3 for brevity. Further discussion about the sensitivity to drag coefficients is presented in Section 5.1.

Since parametric resonance, as discussed in Section 2, depends on the natural periods (T_n) of the system, the numerical model is first used to perform free-decay tests and estimate T_n, shown in Table 4. The change in draft configuration affects mainly the roll and pitch natural periods (23.2 s for D1 and 19.0 s for D2), so that parametric resonance is expected around 11.6 s for D1 and 9.5 s for D2.

5.1. Regular waves tests

The regular wave conditions considered in the experimental campaign are replicated in the numerical model, at full scale. For validation purposes, in order to have the same conditions between numerical and physical models, the free surface elevation recorded from the wave probes in the tank is used as input to the numerical model. In order to replicate the transient and the inherent inaccuracies of the physical wave tank, the regular wave is treated as irregular, i.e., as a combination of a discrete number of regular wave components. Therefore, the pressure and fluid velocity fields, needed for the computation of NLFK and viscous drag forces integrals, also are described as the superposition of different frequency components [52].

Table 4
Natural periods T_n (in seconds) in several DoFs from full-scale numerical simulations of free decay tests for different draft configurations (D1 and D2), as in Section 3.

	Surge & Sway	Heave	Roll & Pitch	Yaw
D1	150	9.8	**23.2**	22.2
D2	150	10.1	**19.0**	23.5

The wave height (H_w) and wave period (T_w) are computed by means of a fast Fourier Transform (FFT), where T_w is the period of highest spectral energy content, and H_w is the mean of the highest 1/3 waves, taken between two consecutive down-crossing of the free surface elevation after the transient period of time. Fig. 12 shows the set of considered waves, highlighting low-amplitude (black squares) and high-amplitude (blue circles) wave conditions, defined with respect to an arbitrary wave height threshold of 2 m.

Figs. 13–16 show a comparison between the numerical and experimental regular-wave results of the time traces of the buoy response. Results in heave, roll, and pitch are presented for the wave conditions highlighted in Fig. 12. Parametric resonance in roll is observed in Fig. 13 (wave condition W1.1), for configuration D1, and in Fig. 14 (wave condition W2.1), for configuration D2. Examples of time traces where parametric roll is not triggered, obtaining a pure heave-pitch response with the same frequency as the incident wave, are provided in Fig. 15 (wave condition W1.2), for configuration D1, and in Fig. 16 (wave condition W2.2), for configuration D2. Pitch results with parametric resonance show an initial response with the same frequency as the incident wave, which changes to half that frequency after the settling of the dynamic instability. The pitch amplitude decreases as the energy is transferred to roll. In all cases, the time series converge to a permanent regime. The settling of roll is captured by the numerical model, even though the maximum amplitude is not reached at the same instant, which may be explained by the unstable nature of the problem and its sensitivity small changes in its parameters. In Fig. 13 and Fig. 14, the heave motion measured during the experimental tests presents a decrease of amplitude after the triggering of the dynamic instability. This decrease is not so clear in the numerical simulations. Finally, some discrepancies are evident in the pitch response, especially in Fig. 13, where the experimental time trace presents an initial rather abrupt increase and decrease of motion, and finally reaches a steady state lower than the one predicted by the numerical model. The main candidate phenomenon of such a response, different from the simulated one, is the coupling with the yaw response, shown in Fig. 17. The excitation of yaw is nonlinear, mainly due to the 3-line mooring system [61], and therefore sensitive to small inaccuracies in the mooring system properties. Once activated, yaw motion is coupled to other DoFs by means of the mooring system, effectively impacting the amplitude of their response.

The response obtained with the numerical model is compared with experimental results, over the whole range of wave conditions shown in Fig. 12, by considering the root mean square (RMS) of the signals after subtracting their mean values (the mean value is denoted by an overline). In this way, only the oscillating part of the signal is considered, as shown in Figs. 17 and 18 for D1 and D2, respectively. Likewise, in Fig. 12, experimental data is shown in black squares and blue circles, indicating small and large waves, respectively. Similarly, numerical results are shown by dot and star markers, respectively. Their colours correspond to different drag coefficient configurations, as in Table 3. Areas where the numerical model detects parametric roll are shaded in light grey.

The region where parametric resonance is detected is consistent with experiments, and agrees with the Mathieu-type instability model, discussed in Section 2. In fact, non-zero roll response is found at about half the roll/pitch natural periods (see Table 4), with higher amplitudes

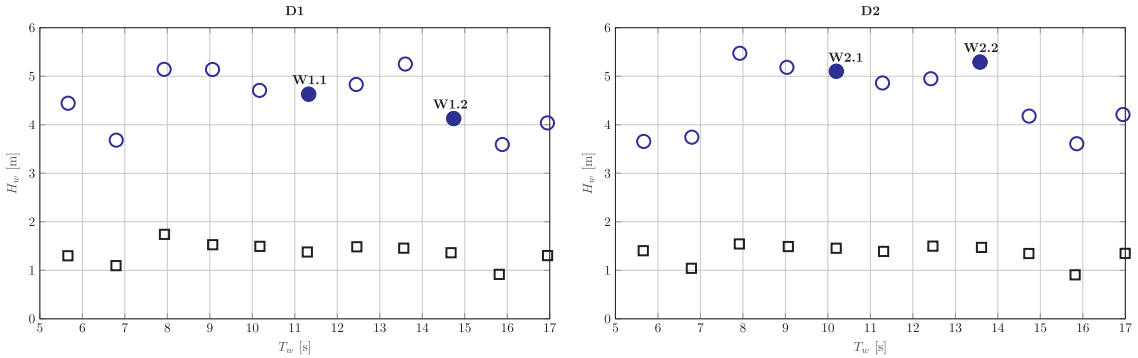

Fig. 12. Wave height H_w as a function of the wave period T_w from the regular-wave experimental tests, for draft configurations D1 (on the left) and D2 (on the right). Black squares represent low-amplitude waves (specified wave height of 1.5 m) and blue circles represent high-amplitude waves (specified wave height of 5.0 m). Examples of time traces of the buoy response to waves W1.1–2 and W2.1–2 are given in Figs. 13–16.

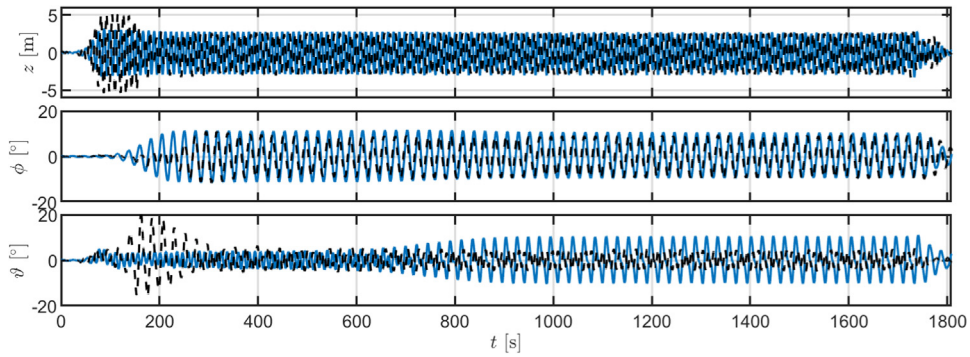

Fig. 13. Heave, roll, and pitch time traces, for configuration D1, for wave condition W1.1 (see Fig. 12). The blue solid lines represent the numerical simulation and the black dashed lines are the experiment.al measurements. (For interpretation of the references to colour in this figure legend, the reader is referred to the web version of this article.)

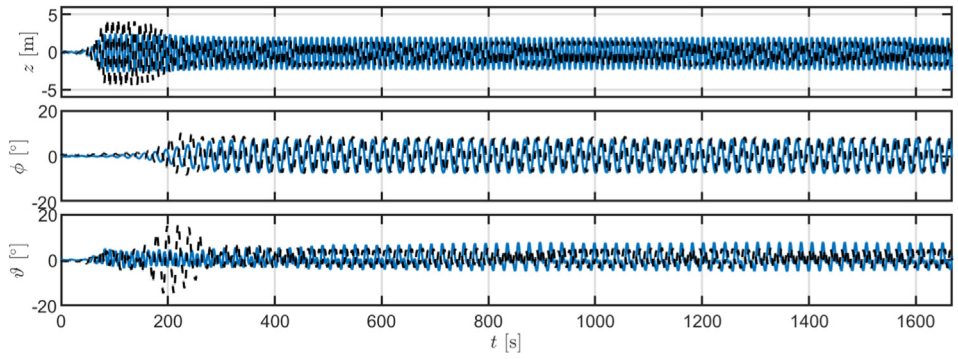

Fig. 14. Heave, roll, and pitch time traces, for configuration D2, for wave condition W2.1 (see Fig. 12). The blue solid lines represent the numerical simulation and the black dashed lines are the experiment.al measurements. (For interpretation of the references to colour in this figure legend, the reader is referred to the web version of this article.)

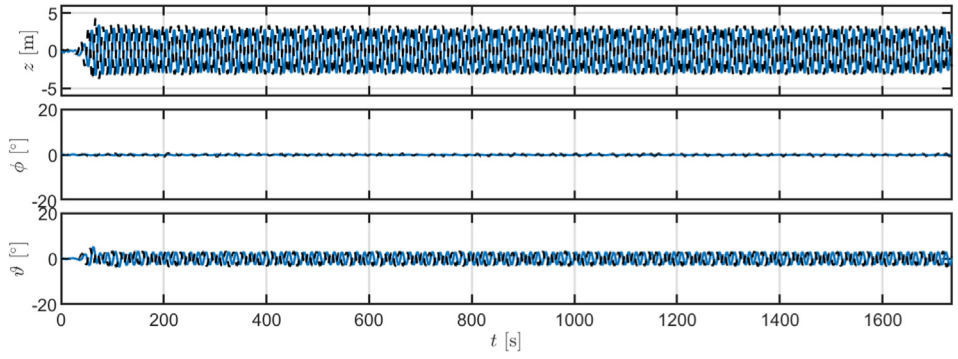

Fig. 15. Heave, roll, and pitch time traces, for configuration D1, for wave condition W1.2 (see Fig. 12). The blue solid lines represent the numerical simulation and the black dashed lines are the experiment.al measurements. (For interpretation of the references to colour in this figure legend, the reader is referred to the web version of this article.)

for configuration D1. However, only large waves cause a significant roll response, since the higher incoming energy exceeds internal dissipations. The severity of parametric resonance is well captured by the numerical model for all three wave conditions within the region of parametric resonance in configuration D2, and for two wave conditions out of three for configuration D1, with an overestimation of the roll amplitude for the wave with the higher period. Comparing the two draft configurations, D2 shows smaller roll responses.

When parametric resonance appears, there is an increase in roll and pitch responses and, consequently, surge and sway, which are coupled

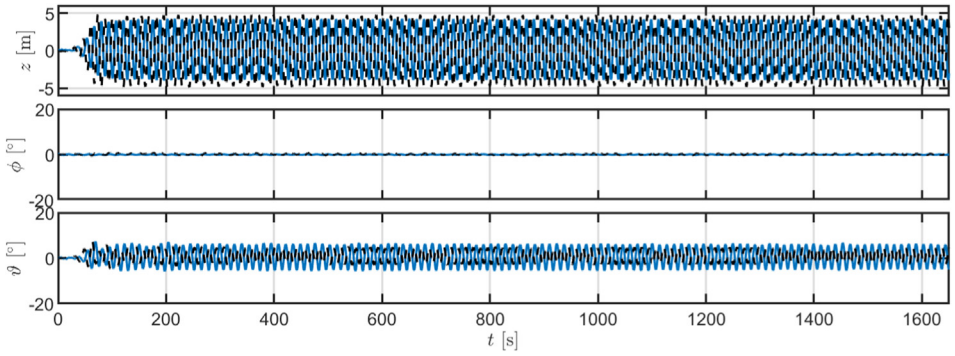

Fig. 16. Heave, roll, and pitch time traces, for configuration D2, for wave condition W2.2 (see Fig. 12). The blue solid lines represent the numerical simulation and the black dashed lines are the experiment.al measurements. (For interpretation of the references to colour in this figure legend, the reader is referred to the web version of this article.)

with the rotational DoFs. The response is due to the nonlinear mooring effects, partially because of coupling between yaw with other DoFs.

Finally, Fig. 17 and 18 show that the nonlinear model produces a satisfactory prediction of the planar motion response (surge-heave-pitch), with higher accuracy for small waves.

The NLFK model is also able to articulate mean drift forces caused by the time-varying wetted surface of surface-piercing bodies [56]. Fig. 19 shows the mean surge displacement caused by drift effects for configurations D1 and D2. Overall, the nonlinear model tends to overestimate the surge displacement. The most likely cause of such an overestimation can be found in the uncertainties concerning the physical and numerical modelling of the mooring system. Due to drift effects, surge is highly dependent on the mooring system, which alone provides the totality of restoring force, since the hydrodynamic stiffness is null in the surge DoF. Consequently, discrepancies between the physical tests and the mathematical model of the mooring system are potentially hindering a correct reproduction of the mean drift displacement. Such discrepancies may be due to either an over-simplified mathematical model and to measuring inaccuracies during the experimental campaign.

In order to assess the quality of mooring loads reproduction, the quasi-static mooring model is run independently from the hydrodynamic code by directly feeding the model with the kinematics recorded during the experiments. In this way, having the same kinematics in both the physical and numerical environments, differences between measured and predicted tensions can be ascribed only to the representativeness of the mathematical model and the accuracy of experimental measures. Figs. 20 and 21 compare the mean and RMS tension at the fairleads of each one of the three mooring lines. Note that, before computing the mean and RMS, the pretension T_0 has been subtracted from the total fairlead tension T_m.

Overall, as expected due to the mean drift effect, average and RMS tensions on the front line (ML1) are larger than on the rear lines (ML2 and ML3). A reasonably good agreement is found, between numerical prediction and experimental measures, with higher accuracy for small waves. However, relatively small differences in the mooring tension can have a great impact on the mean surge displacement, since mooring lines are the only elements providing a restoring effect in surge. This reasoning is consistent with the discrepancies found in Fig. 19.

5.2. Computational time

Although this paper implements a computationally convenient model, the main purpose is validation and detection of parametric resonance, as opposed to computational time minimization. Therefore, the computational times presented in this section should be considered as suboptimal. However, this section presents a discussion on the most important aspects determining the overall computational burden, the description of the setup considered in this paper, and recommendation on possible ways to potentially decrease the computational time with no significant loss of accuracy.

The first trivial but most important parameter in determining the total computational time is the time step, whose selection is led by a convergence analysis and an arbitrary choice of computation/accuracy compromise. In this work, as discussed in Section 4.1, δt is chosen equal to $T_p/50$.

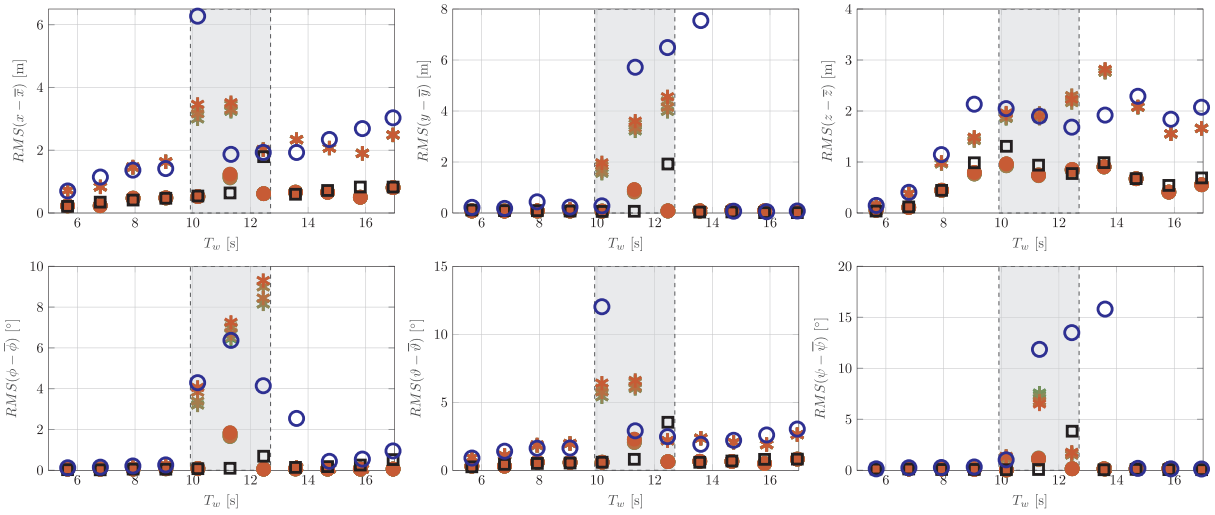

Fig. 17. Root mean square (RMS) of the oscillating response (after subtracting its mean), for draft configuration D1. Experimental results are shown with the same markers as in Fig. 12, while simulated results are shown by disks and asterisks, for small and large waves, respectively. Different colours refer to different drag coefficient combinations, as in Table 3.

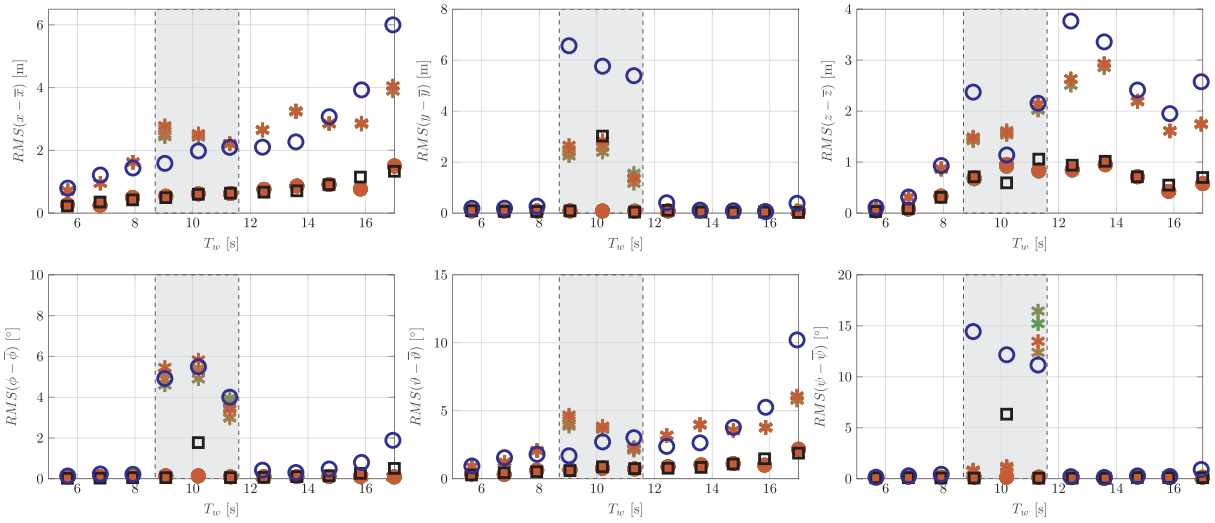

Fig. 18. Root mean square (RMS) of the oscillating response (after subtracting its mean), for draft configuration D2. Experimental results are shown with the same markers as in Fig. 12, while simulated results are shown by disks and asterisks, for small and large waves, respectively. Different colours refer to different drag coefficient combinations, as in Table 3.

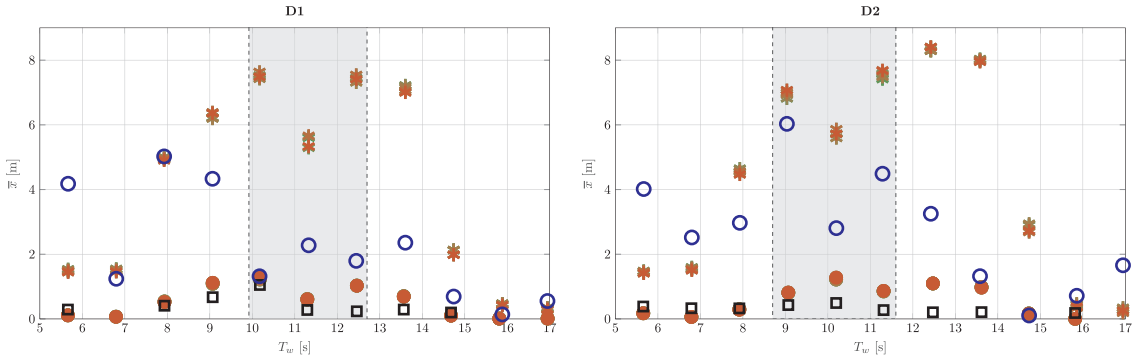

Fig. 19. Mean surge displacement caused by drift effects for draft configuration D1 (on the left) and D2 (on the right). Experimental results are shown with the same markers as in Fig. 12, while simulated results are shown by disks and asterisks, for low-amplitude and high-amplitude waves, respectively. Different colours refer to different drag coefficient combinations, as in Table 3. The shaded areas refer to regions where the numerical model detects parametric resonance, as shown in Figs. 17 and 18.

At each time step, the computational time is driven by the calculation of numerical integrals, mainly for NLFK forces (requiring two-dimensional integrals), and secondly for viscous drag forces (requiring one-dimensional integrals). Such a computational time depends on how many integrals are computed and on the required accuracy of their approximation. The number of integrals depends on the number and type of sections, and the number of DoFs, as discussed in Section 4.2.1. In this work, the full complexity of the buoy has been considered, comprising of 12 sections in total (5 cylinders, 4 cones, 2 torus, 1 disk). However, some of the sections are relatively small and/or deep, so that

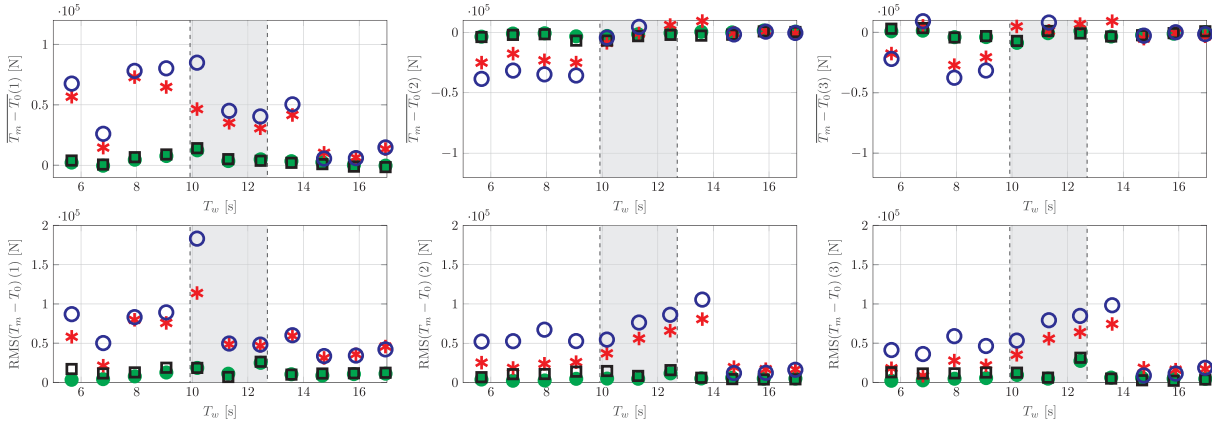

Fig. 20. Mean (top) and root mean square (bottom) values of the tension of the three mooring lines (front line ML1 on the left, rear lines ML2 and ML3 in the middle and on the right, respectively), for draft configuration D1. Experimental results are shown with the same markers as in Fig. 12, while simulated results are shown by disks and asterisks, for small and large waves, respectively.

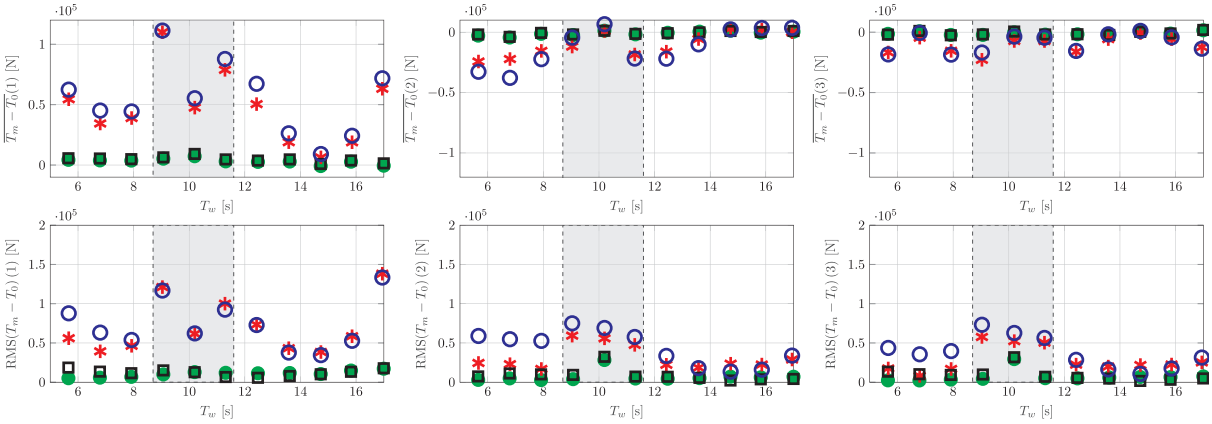

Fig. 21. Mean (top) and root mean square (bottom) values of the tension of the three mooring lines (front line ML1 on the left, rear lines ML2 and ML3 in the middle and on the right), for draft configuration D2. Experimental results are shown with the same markers as in Fig. 12, while simulated results are shown by disks and asterisks, for small and large waves, respectively, as in Figs. 17 and. 18.

their contributions are potentially negligible, while significantly affecting the overall computational burden.

Another major parameter determining the computational time of the numerical integration is the required accuracy of the approximation, defined by the relative and absolute tolerances [58]. In this work, for sake of simplicity and accuracy, the same tolerances are assumed for all simulations and DoFs, and through the whole time simulation (absolute tolerance of 10 and relative tolerance of 0.005). Nevertheless, a potential way to reduce the unnecessary computational time with no relevant effect on the accuracy is to adopt an appropriate strategy to modify the tolerances in a sensible way, depending on either the sea state, the values of the displacements of each DoF, and/or the values of the integral at the previous time step. However, this has not been investigated in this paper.

Finally, Fig. 22 shows the relative computational time (t_{rel}) for both draft configurations, where t_{rel} is defined as the ratio between run-time and computational time. If $t_{rel} = 1$, the simulation run in real-time, while it is slower than real time if $t_{rel} > 1$. Calculations have been performed on a dedicated high-performance computer at Politecnico di Torino (HPC@Polito), each simulation on a single core with CPU 2x Xeon E5-2680 v3 2.50 GHz. The resulting relative computational time in Fig. 22 varies from a minimum of 2.84 to a maximum of 9.53, with a mean of 4.93 and standard deviation of 1.82. In the attempt to preliminarily justify such variations, t_{rel} is plotted against the root mean square of the different DoFs, showing a correlation between the increase of heave (mainly) and surge/pitch (secondly), and the decrease of computational time. On the other hand, when roll, sway, and yaw become non-zero (when parametric resonance arises), the computational time is always relatively low. Therefore, a plausible explanation could be that the constant tolerances affect the rate of convergence of the numerical integration in a different way according to the magnitude of the displacements in the different DoFs, i.e. the magnitude of Froude-Krylov and drag forces. Therefore a conditional definition of numerical integration tolerances, as opposed to constant, is likely to have the potential to decrease the computational time. However, further investigation (outside the scope of this paper) is necessary to fully justify the correlation shown in Fig. 22.

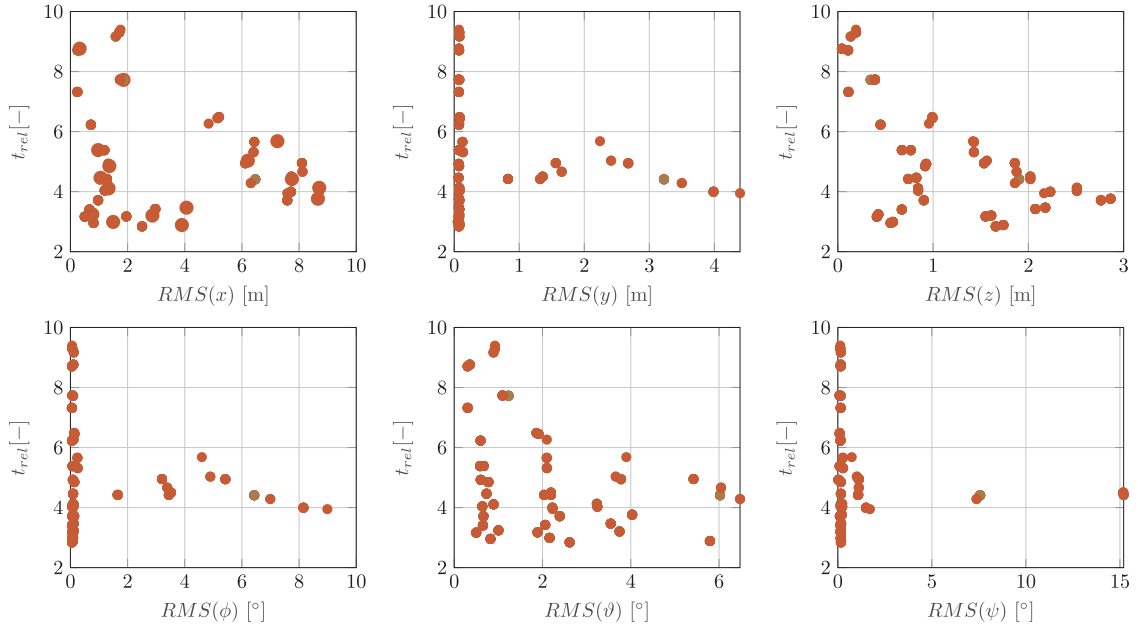

Fig. 22. Relative computational time for both draft configurations, defined as the ratio between run-time and simulation time. Maximum value: 9.53; minimum value: 2.84; mean value: 4.93; standard deviation 1.82.

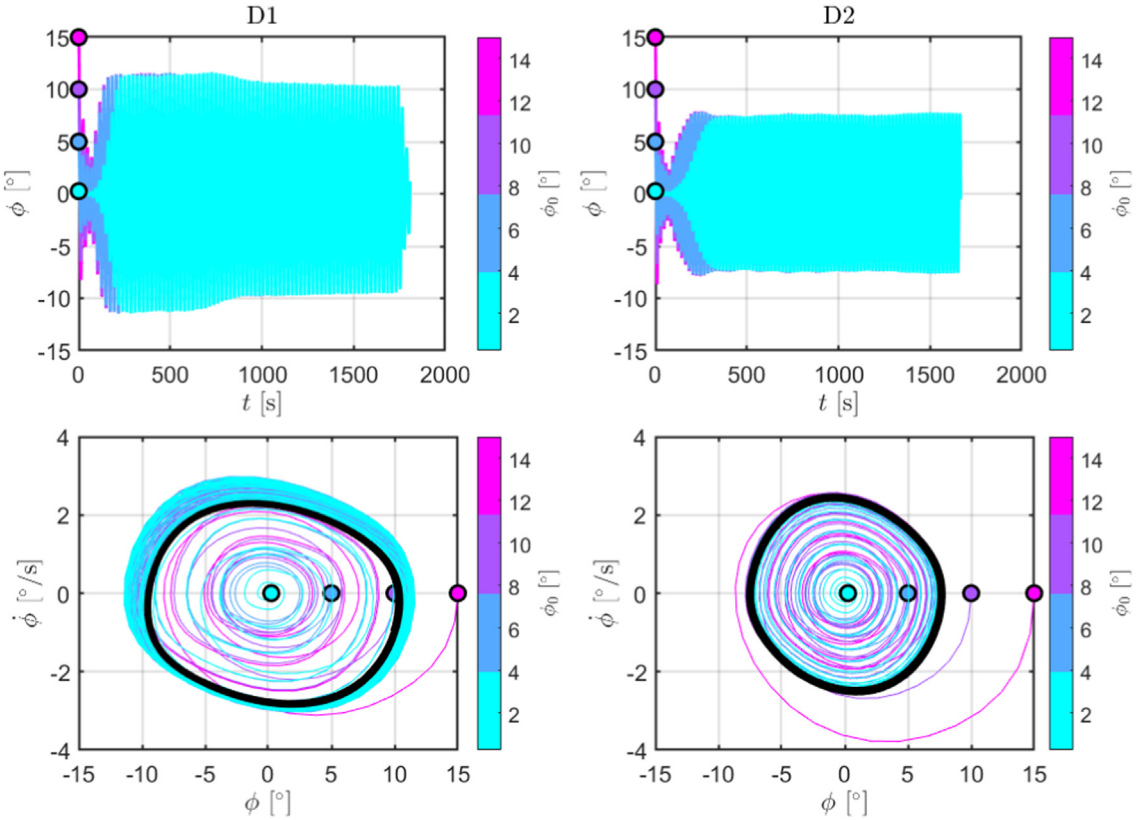

Fig. 23. Time traces (top) and phase portraits (bottom), for configuration D1 with wave W1.1 (left), and configuration D2 with wave W2.1 (right), for four different initial conditions (ϕ = 0.25°, 5°, 10°, 15°). The thick black line represents the steady limit cycle, which is the same for all initial conditions.

5.3. Discussion

This subsection purports to analyse and discuss with greater detail the nonlinear behaviour of the system and its consequences on energy generation. Systems with evident nonlinear dynamics should be studied under different initial conditions, since multiple limit cycles and periodic attractors may arise, depending on the initial state from where the system is perturbed. Fig. 23 shows that the system studied in this paper reaches the same roll limit cycle, regardless of the initial roll angle. Note that the initial conditions are chosen both inside and outside of the steady limit cycle. The only impact of different initial roll angles on the system response is the duration of the transient before reaching the permanent regime.

It is worth to reconstruct the stability diagram (Δ versus Λ) from numerical simulations, and compare it with the analytical prediction of the simplified Mathieu-Eq. 1-DoF model, shown in Fig. 1. Figs. 24 and 25 present such a stability diagram, derived from the 1-DoF model described in Section 2, where the time-variations of the hydrostatic stiffness are computed using the 6-DoF displacements predicted by the NLFK model. The instantaneous metacentric height and submerged volume are computed through integration within the NLFK framework [59]. A comprehensive set of regular waves is considered, with T_w ranging from 5 s to 20 s, with step of 0.25 s, and H_w ranging from 0.5 m to 5 m, with an interval of 0.5 m. The dimensionless damping coefficient μ is obtained through the linearization of the damping forces acting in roll (due to wave radiation and viscous fluid effects) [62], and is frequency dependent. Fig. 24 shows the results for configuration D1, while configuration D2 is presented in Fig. 25. The points with the larger amplitudes in roll are located inside the stable region. Most points outside the unstable region present either small or negligible roll amplitudes. The high roll amplitudes outside the unstable region are found for the higher amplitude waves, where the damping linearization becomes less adequate. These points tend to appear for Δ values on the left side of the stability region. Overall, the stability diagram based on the damped Mathieu equation appears to be an adequate tool to detect the occurrence of roll parametric resonance.

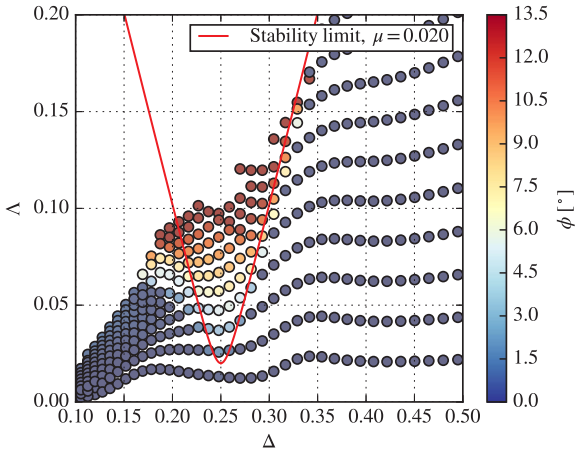

Fig. 24. Stability diagram (Δ versus Λ) for the first instability zone, as described in Section 2, for configuration D1. The colour of the markers is proportional to the roll amplitude.

Fig. 26 presents numerical results of the capture width ratio (CWR) versus the incident wave period T_w. Numerical simulations of the experimental tests are represented by black disks and the asterisks, while the solid lines are obtained through numerical simulation of regular waves with a constant H_w and considering a refined range of wave periods. The nonlinear effect is clearly visible in both graphs through the observation of the differences between lines tests with different wave height. Beyond parametric resonance, nonlinearities may be caused by the turbine damping effect and by the viscous fluid effects.

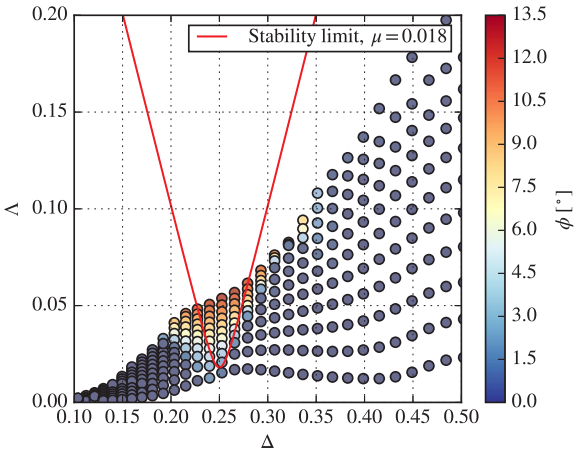

Fig. 25. As in Fig. 24, for configuration D2.

The detrimental effect of parametric resonance on the energy conversion efficiency can be assessed numerically by considering the power extracted with and without the evaluation of nonlinear Froude-Krylov forces. The time-averaged extracted power ($\overline{\mathscr{P}}$) is presented on the top part of Fig. 27, which shows a sharp decrease around half the roll/pitch natural period, where parametric resonance is expected to occur. In the bottom part of Fig. 27, $\Delta\overline{\mathscr{P}}$ represents the relative difference between the predicted mean extracted power with linear and nonlinear Froude-Krylov forces, while all other nonlinearities remain the same. Note that $\Delta\overline{\mathscr{P}} < 0$ means that the predicted power in the NLFK model is lower. It is clear that neglecting Froude-Krylov force nonlinearities when parametric resonance occurs causes a significant overestimation of the power production. Conversely, a beneficial effect is found for configuration D2 for large waves at a period of about 12 s, which is due to the water column dynamics. At the side of each $\Delta\overline{\mathscr{P}}$ map, there is the percentage normalized difference, computed as the ratio between $\Delta\overline{\mathscr{P}}$ and $\overline{\mathscr{P}}$. Note that such a ratio is not meaningful if computed in areas where $\overline{\mathscr{P}}$, at the denominator, is too small. Therefore, this ratio is shown only for the wave period of greatest interest where parametric resonance occurs while the produced power is not negligible. A peak of 53% difference is obtained for a wave height of 3 m, effectively providing an evident and quantitative measure of the detrimental effects of parametric resonance.

6. Conclusions

The accurate numerical simulation of wave energy converters requires capturing a vast range of phenomena that affect their dynamics. Roll parametric resonance is a highly nonlinear phenomenon originated by a dynamic instability that can affect, mainly but not limited to, spar-type heaving wave energy converters. Probably due to the complexity of the model required to assess this instability, few works have been dedicated to this issue.

In this paper we presented the validation of numerical results using a 6-degree of freedom nonlinear Froude-Krylov model using data from experimental model-scale tests of a Spar-buoy oscillating water column device subject to regular wave conditions. The mooring system was modelled in detail using a quasi-static model and drag forces, due to viscous fluid effects, are considered for a more realistic simulation of the system damping. Two mass distribution configurations of the Spar-buoy oscillating water column are studied, which represent two different cases for the study of parametric resonance. For both configurations, the model was able to detect roll parametric resonance in all tests except one, located at the border of the unstable region. This can be justified by small inaccuracies in the model inputs, since this phenomenon is sensitive to small changes in its parameters. The reduction in heave that is observed in the experiments after the triggering of roll parametric resonance was not so evident in the numerical simulations. These discrepancies may be associated with the model not accounting for all hydrodynamics effect of the water column, e.g. damping due to sloshing. Stability diagrams, based on the damped Mathieu equation, are commonly used to assess the occurrence of roll parametric resonance through the evaluation of the hydrostatic stiffness variation. This simplified model was able to detect the zones of large roll amplitudes obtained by the nonlinear Froude-Krylov model with a reasonable accuracy, which shows its applicability for design purposes, where less detail is required. Using the numerical model, we were able to evaluate the negative impact that parametric resonance has on the power extraction. For a wave with a height of 3 m, a maximum reduction of 53% on power performance due to parametric resonance was found.

This work presented an extensive validation of numerical results with parametric resonance. Novelties in this study included the consideration of viscous fluid effects on the buoy and a detailed description of the mooring lines. Both effects are relevant for assessing the buoy dynamics under roll parametric resonance. A more comprehensive description of the hydrodynamic effects inside the water column is likely to provide an improvement on the accuracy of the numerical model, which can be the subject of a future work.

CRediT authorship contribution statement

Giuseppe Giorgi: Conceptualization, Methodology, Software, Formal analysis, Resources, Data curation, Writing - original draft, Writing - review & editing, Visualization, Project administration, Funding acquisition. **Rui P.F. Gomes:** Conceptualization, Methodology, Software, Formal analysis, Resources, Data curation, Writing - original draft, Writing - review & editing, Visualization, Project administration, Funding acquisition. **João C.C. Henriques:** Conceptualization, Resources, Supervision, Project administration,

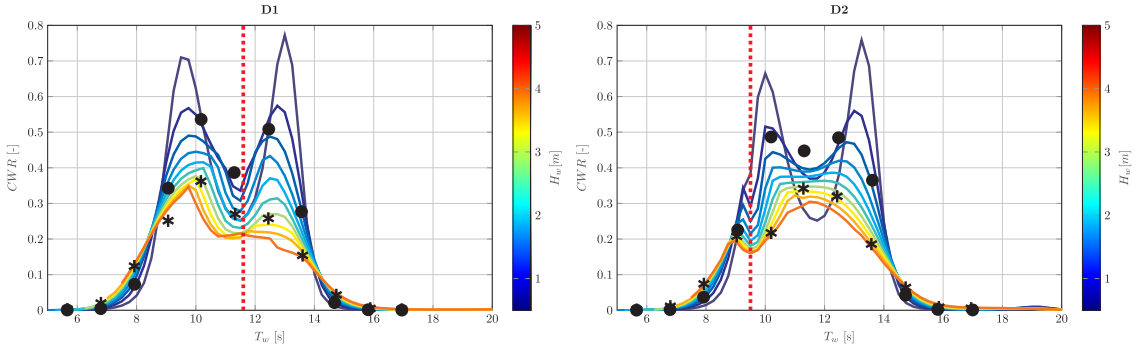

Fig. 26. Capture width ratio (CWR) as a function of the incident wave period T_w, for configuration D1 (left) and D2 (right). The black disks and the asterisks represent results from numerical simulations of the experimental tests, as in shown in Figs. 17 and 18. The continuous lines represent numerical regular wave simulations with different wave height H_w. The dashed line is located at half the roll/pitch natural period.

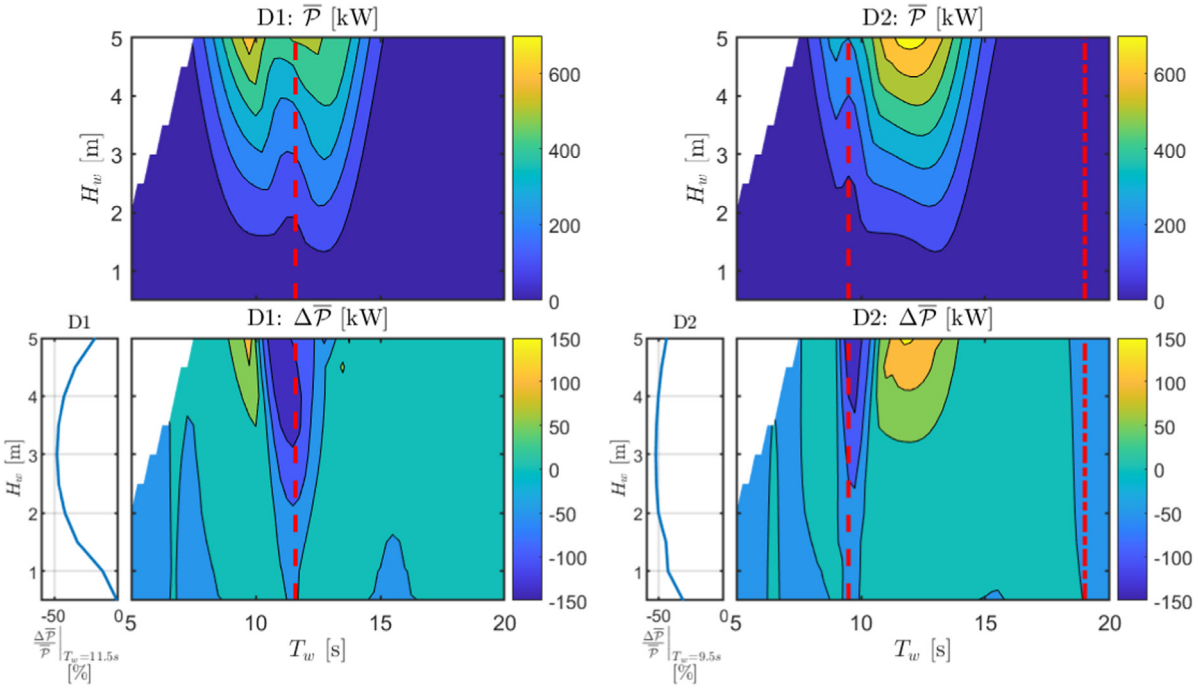

Fig. 27. On the top: mean extracted power ($\overline{\mathcal{P}}$) according to the nonlinear model; on the bottom: difference ($\Delta\overline{\mathcal{P}}$) between the mean extracted power with linear and nonlinear Froude-Krylov force calculation (all nonlinearities remain the same). The dashed line is located at half the roll natural period. At the side of each $\Delta\overline{\mathcal{P}}$ map, there is the percentage normalized difference ($\Delta\overline{\mathcal{P}}/\overline{\mathcal{P}}$) computed at periods equal to half the roll natural period.

Funding acquisition. **Luís M.C. Gato:** Conceptualization, Resources, Supervision, Project administration, Funding acquisition. **Giovanni Bracco:** Conceptualization, Resources, Supervision, Project administration, Funding acquisition. **Giuliana Mattiazzo:** Conceptualization, Resources, Supervision, Project administration, Funding acquisition.

Declaration of Competing Interest

The authors declare that they have no known competing financial interests or personal relationships that could have appeared to influence the work reported in this paper.

Acknowledgements

This research has received funding from the European Research Executive Agency (REA) under the European Unions Horizon 2020 research and innovation programme under grant agreement No 832140. The present research work was also partially funded by Portuguese Foundation for Science and Technology (FCT), through IDMEC, under LAETA project UIDB/50022/2020. The access to Plymouth University large ocean basin was financed by the European Commission's Seventh Framework Programme under MARINET (Marine Renewables Infrastructure Network) initiative, grant agreement No. 262552. Computational re-sources provided by hpc@polito (http://hpc.polito.it).

References

[1] Fossen TI, Nijmeijer H, editors. Parametric resonance in dynamical systems. New York, USA: Springer; 2012.
[2] Eatock Taylor R, Knoop J. Dynamic instability of a freely floating platform in waves. In: Armer GST, Garas FK, editors. Design for dynamic loading - the use of model analysis. Construction Press; 1982. p. 57–62.
[3] France WN, Levadou M, Treakle TW, Paulling JR, Michel RK, Moore C. An investigation of head-sea parametric rolling and its influence on container lashing systems. In: SNAME annual meeting 2001 presentation. 2001.
[4] Shin Y, Belenky V, Paulling J, Weems K, Lin W. Criteria for parametric roll of large containerships in longitudinal seas. Soc Naval Archit Marine Eng 2004;112:14–47.
[5] Umeda N, Hashimoto H, Vassalos D, Urano S, Okou K. Nonlinear dynamics on parametric roll resonance with realistic numerical modelling. Int Shipbuilding Progress 2004;51:205–20.
[6] Rodríguez CA, Neves MAS. Nonlinear instabilities of spar platforms in waves. In: Proc. of the 31st International Conference on Ocean, Offshore and Arctic Engineering. Rio de Janeiro, Brazil; 2012.
[7] Rho JB, Choi HS, Shin HS, Park IK. A study on Mathieu-type instability of conventional spar platform in regular waves. Int J Offshore Polar Eng 2005;15(02):104–8.
[8] Li BB, Ou JP, Teng B. Numerical investigation of damping effects on coupled heave and pitch motion of an innovative deep draft multi-spar. J Mar Sci Technol 2011;19(2):231–44.
[9] Robertson B, Bekker J, Buckham B. Renewable integration for remote communities: Comparative allowable cost analyses for hydro, solar and wave energy. Appl Energy 2020;264:114677. https://doi.org/10.1016/J.APENERGY.2020.114677.
[10] Sheng W, Flannery B, Lewis A, Alcorn R. Experimental studies of a floating cylindrical OWC WECs. In: Proc. of the 31st International Conference on Ocean, Offshore and Arctic Engineering. Rio de Janeiro, Brazil; 2012.
[11] Payne GS, Taylor JRM, Bruce T, Parkin P. Assessment of boundary-element method for modelling a free-floating sloped wave energy device. Part 1: Numerical modelling. Ocean Eng 2008;35(3–4):333–41. https://doi.org/10.1016/j.oceaneng.2007.10.006.
[12] Tarrant K, Meskell C. Investigation on parametrically excited motions of point absorbers in regular waves. Ocean Eng 2016;111:67–81. https://doi.org/10.1016/j.oceaneng.2015.10.041.
[13] Correia da Fonseca F, Gomes R, Henriques J, Gato L, Falcão A. Model testing of an oscillating water column spar-buoy wave energy converter isolated and in array: Motions and mooring forces. Energy 2016;112:1207–18. https://doi.org/10.1016/j.energy.2016.07.007.
[14] Gomes RPF, Malvar Ferreira JDC, Ribeiro e Silva S, Henriques JCC, Gato LMC. An experimental study on the reduction of the dynamic instability in the oscillating water column spar buoy. In: Proc. of the 9th European Wave and Tidal Energy Conference. Cork, Ireland; 2017.
[15] Babarit A, Mouslim H, Clement A, Laporte-Weywada P. On the numerical modelling of the non linear behavior of a wave energy converter. In: 28th International Conference on Ocean, Offshore and Arctic Engineering. Honolulu, Hawaii, USA; 2009.
[16] Giorgi Giuseppe, Gomes Rui PF, Bracco Giovanni, Mattiazzo Giuliana. Numerical investigation of parametric resonance due to hydrodynamic coupling in a realistic wave energy converter. Nonlinear Dyn 2020. https://doi.org/10.1007/s11071-020-05739-8.
[17] Giorgi G, Ringwood JV. A compact 6-DoF nonlinear wave energy device model for power assessment and control investigations. IEEE Trans Sustainable Energy 2019;10(1):119–26. https://doi.org/10.1109/TSTE.2018.2826578.
[18] Palm J, Bergdahl L, Eskilsson C. Parametric excitation of moored wave energy converters using viscous and non-viscous CFD simulations. In: Soares, C.G., editor. Advances in Renewable Energies Offshore. Taylor & Francis Group, 2019. ISBN 978-1-138-58535-5; 2019.
[19] Son D, Yeung RW. Optimizing ocean-wave energy extraction of a dual coaxial-cylinder WEC using nonlinear model predictive control. Appl Energy

2017;187:746–57. https://doi.org/10.1016/J.APENERGY.2016.11.068.
[20] Zhang H, Zhou B, Vogel C, Willden R, Zang J, Geng J. Hydrodynamic performance of a dual-floater hybrid system combining a floating breakwater and an oscillating-buoy type wave energy converter. Appl Energy 2020;259:114212. https://doi.org/10.1016/J.APENERGY.2019.114212.
[21] Elhanafi A, Macfarlane G, Fleming A, Leong Z. Experimental and numerical investigations on the hydrodynamic performance of a floating–moored oscillating water column wave energy converter. Appl Energy 2017;205:369–90. https://doi.org/10.1016/J.APENERGY.2017.07.138.
[22] Falcão A, Henriques J. Oscillating-water-column wave energy converters and air turbines: A review. Renew Energy 2016;85:1391–424. https://doi.org/10.1016/j.renene.2015.07.086.
[23] Falcão AFO, Henriques JCC, Gato LMC. Self-rectifying air turbines for wave energy conversion: A comparative analysis. Renew Sust Energy Rev 2018;85:1391–424. https://doi.org/10.1016/j.renene.2015.07.086.
[24] McCormick ME. Modified linear-analysis of a wave-energy conversion buoy. Ocean Eng 1976;3(3):133–44.
[25] Masuda Y. An experience of wave power generator through tests and improvment. In: Evans, D.V., Falcão, A.F. de O., editors. Hydrodynamics of Ocean Wave Energy Utilization Symposium. Lisbon, Portugal; 1985.
[26] Whittaker TJT, McPeake FA. Design optimization of axi-symmetric tail tube buoys. In: Evans, D.V., Falcão, A.F. de O., editors. Hydrodynamics of Ocean Wave Energy Utilization Symposium. Lisbon, Portugal; 1985.
[27] Alves MA, Costa IR, Sarmento AJNA, Chozas JF. Performance evaluation of an axysimmetric floating OWC. In: Proc. of the 20th International Offshore and Polar Engineering Conference. Beijing, China; 2010.
[28] Gomes RPF, Henriques JCC, Gato LMC, Falcão AFO. Hydrodynamic optimization of an axisymmetric floating oscillating water column for wave energy conversion. Renew Energy 2012;44:328–39. https://doi.org/10.1016/j.renene.2012.01.105.
[29] Falcão AFO, Henriques JCC, Cândido JJ. Dynamics and optimization of the OWC spar buoy wave energy converter. Renew Energy 2012;48:369–81. https://doi.org/10.1016/j.renene.2012.05.009.
[30] Simonetti I, Cappietti L, Oumeraci H. An empirical model as a supporting tool to optimize the main design parameters of a stationary oscillating water column wave energy converter. Appl Energy 2018;231:1205–15. https://doi.org/10.1016/J.APENERGY.2018.09.100.
[31] Gomes RPF, Henriques JCC, Gato LMC, Falcão AFO. Wave power extraction of a heaving floating oscillating water column in a wave channel. Renew Energy 2016;99:1262–75. https://doi.org/10.1016/j.renene.2016.08.012.
[32] Gomes RPF, Henriques JCC, Gato LMC, Falcão AFO. Time-domain simulation of a slack-moored floating oscillating water column and validation with physical model tests. Renewable Energy 2020;149:165–80. https://doi.org/10.1016/J.RENENE.2019.11.159.
[33] Faltinsen OM. Sea loads on ships and offshore structures. Cambridge University Press; 1990.
[34] Chakrabarti, S., editor. Handbook of offshore engineering: volume I. Elsevier Ltd.; 2005.
[35] Grimshaw R. Nonlinear ordinary differential equations. USA: CRC Press; 1993.
[36] Jordan DW, Smith P. Nonlinear ordinary differential equations: an introduction for scientists and engineers. 4th ed. New York, USA: Oxford University Press; 2007.
[37] Hughes SA. Physical models and laboratory techniques in coastal engineering. World Scientific Publishing; 1993.
[38] Pozzi N, Bracco G, Passione B, Sirigu SA, Mattiazzo G. PeWEC: Experimental validation of wave to PTO numerical model. Ocean Eng 2018;167:114–29. https://doi.org/10.1016/J.OCEANENG.2018.08.028. URL https://www.sciencedirect.com/science/article/pii/S0029801818315233?via%3Dihub.
[39] Sirigu SA, Bonfanti M, Passione B, Begovic E, Bertorello C, Dafnakis P, et al. Experimental investigation of the hydrodynamic performance of the ISWEC 1: 20 scaled device. NAV International Conference on Ship and Shipping Research. 221499 2018. p. 551–60. https://doi.org/10.3233/978-1-61499-870-9-551.
[40] Giorgi G, Gomes RPF, Bracco G, Mattiazzo G. The effect of mooring line parameters in inducing parametric resonance on the Spar-buoy oscillating water column wave energy converter. J f Marine Sci Eng 2020;8(1):1–20. https://doi.org/10.3390/JMSE8010029.
[41] Penalba M, Davidson J, Windt C, Ringwood JV. A high-fidelity wave-to-wire simulation platform for wave energy converters: Coupled numerical wave tank and power take-off models. Appl Energy 2018;226:655–69. https://doi.org/10.1016/J.APENERGY.2018.06.008.
[42] Giorgi G, Ringwood JV. Analytical formulation of nonlinear Froude-Krylov forces for surging-heaving-pitching point absorbers. In: ASME 2018 37th International Conference on Ocean, Offshore and Arctic Engineering. Madrid; 2018b.
[43] Giorgi G, Ringwood JV. Articulating parametric nonlinearities in computationally efficient hydrodynamic models. In: Proceedings of the 11th IFAC Conference on Control Applications in Marine Systems, Robotics, and Vehicles. Opatija; 2018c.
[44] Windt C, Davidson J, Ringwood JV. High-fidelity numerical modelling of ocean wave energy systems: A review of computational fluid dynamics-based numerical wave tanks. Renew Sustain Energy Rev 2018;93(April):610–30. https://doi.org/10.1016/j.rser.2018.05.020.
[45] Abbasnia A, Guedes Soares C. Fully nonlinear simulation of wave interaction with a cylindrical wave energy converter in a numerical wave tank. Ocean Eng June 2016;2018(152):210–22. https://doi.org/10.1016/j.oceaneng.2018.01.009.
[46] Michele S, Sammarco P, D'Errico M. Weakly nonlinear theory for oscillating wave surge converters in a channel. J Fluid Mech 2018;834:55–91. https://doi.org/10.1017/jfm.2017.724.
[47] Wendt F, Nielsen K, Yu YH, Bingham H, Eskilsson C, Kramer B. et al. Ocean Energy Systems wave energy modeling task: modeling, verification, and validation of wave energy converters. J Marine Sci Eng. 2019;7(379):1–22. doi: 10.3390/jmse7110379.
[48] Gilloteaux JC. Large amplitude motions of floating bodies in potential theory. application to wave energy conversion. Ph.D. thesis; École Centrale de Nantes; 2007.
[49] Giorgi G, Ringwood JV. Analytical representation of nonlinear Froude-Krylov forces for 3-DoF point absorbing wave energy devices. Ocean Eng 2018;164(2018):749–59. https://doi.org/10.1016/j.oceaneng.2018.07.020.
[50] Giorgi G, Ringwood JV. Parametric motion detection for an oscillating water column spar buoy. In: Proceedings of the 3rd International Conference on Renewable Energies Offshore RENEW. Lisbon; 2018e.
[51] Giorgi G, Ringwood JV. Articulating parametric resonance for an OWC spar buoy in regular and irregular waves. J Ocean Eng Marine Energy 2018;4(4):311–22. https://doi.org/10.1007/s40722-018-0124-z.
[52] WAMIT I. WAMIT User Manual. 2019. doi:10.1017/CBO9781107415324.004.
[53] Penalba M, Kelly TE, Ringwood JV. Using NEMOH for modelling wave energy converters: a comparative study with WAMIT. In: Proceedings of the 12th European Wave and Tidal Energy Conference; 2017.
[54] Ogilvie TF. Recent progress toward the understanding and prediction of ship motions. In: Proc. of the 5th Symposium on Navan Hydrodynamics; vol. ACR-112 of ONR. Bergen; 1964, p. 3–79.
[55] Faedo N, Peña-Sanchez Y, Ringwood JV. Finite-order hydrodynamic model determination for wave energy applications using moment-matching. Ocean Eng 2018;163:251–63.
[56] Fossen TI. Handbook of marine craft hydrodynamics and motion control. John Wiley & Sons; 2011.
[57] Giorgi G, Ringwood JV. Relevance of pressure field accuracy for nonlinear Froude-Krylov force calculations for wave energy devices. J Ocean Eng Marine Energy 2018;4(1):57–71. https://doi.org/10.1007/s40722-017-0107-5.
[58] Shampine LF. Matlab program for quadrature in 2D. Appl Math Comput 2008;202(1):266–74. https://doi.org/10.1016/j.amc.2008.02.012.
[59] Giorgi G. Nonlinear Froude-Krylov Matlab demonstration toolbox; 2019. doi: 10.5281/zenodo.3544848.
[60] Falcão AFO, Henriques JCC. The spring-like air compressibility effect in oscillating-water-column wave energy converters: Review and analyses. Renew Sustain Energy Rev 2019;112:483–98.
[61] Orszaghova J, Wolgamot H, Draper S, Taylor PH, Rafiee A. Onset and limiting amplitude of yaw instability of a submerged three-tethered buoy. Proc Roy Soc A: Mathe, Phys Eng Sci 2020. https://doi.org/10.1098/rspa.2019.0762.
[62] Terra GM, Jan van de Berg W, Maas LRM. Experimental verification of Lorentz linearization procedure for quadratic friction. Fluid Dyn Res 2005;36:175–88.